

# A co-volume scheme for the rotating shallow water equations on conforming non-orthogonal grids

Qingshan Chen<sup>a</sup>, Todd Ringler<sup>a</sup>, Max Gunzburger<sup>b</sup>

<sup>a</sup>*Theoretical Division, T-3, Los Alamos National Laboratory, Los Alamos, NM 87545*

<sup>b</sup>*Department of Scientific Computing, Florida State University, Tallahassee, FL 32306*

---

## Abstract

A co-volume scheme is introduced for the rotating shallow water equations, in which both velocity components are specified on cell edges, and the thickness variables evolve on both the primary and the dual cell centers. The scheme applies to generic, conforming and non-orthogonal staggered grids, including the widely used lat-lon quadrilateral grids and the Delaunay-Voronoi tessellations. It can be viewed either as coupled C-grid schemes on the primary and dual meshes, or as an generalization of the traditional E-grid scheme on a new non-overlapping grid. Linear dispersive wave analysis shows that, on the wavenumber space resolved by either the primary or the dual mesh of a uniform quadrilateral staggered grid, the co-volume scheme possesses the same dispersive relations as the Z-grid scheme. The total wavenumber space resolved by the staggered grid is twice as large, on which the co-volume behaves exactly like the E-grid scheme. On a uniform hexagon-triangular staggered grid, the co-volume has two steady modes and two inertial-gravity modes on the hexagonal mesh, and one steady mode, two inertial gravity modes, and two spurious modes on the triangular mesh. On the wavenumber space resolved by either the hexagonal or the triangular mesh, the inertial-gravity wave modes remain positive and largely monotone. For the nonlinear shallow water equations, the co-volume scheme is shown to preserve the potential vorticity dynamics and the total energy exactly. Numerical results are presented to corroborate and supplement the analyses.

*Keywords:* co-volume, finite volume method, shallow water equations, computational modes, unstructured grid, non-orthogonal grid

---

## 1. Introduction

Primary concerns in designing numerical algorithms for geophysical flows are evaluating the method’s ability to faithfully simulate linear wave dynamics and conserve certain system invariants such as global mass, potential vorticity and total energy in the nonlinear system. A robust accounting for global invariants is particularly important when simulating geophysical flows on climate or climate change time scales which may span hundreds or thousands of years. For climate applications, C-grid ([2]) schemes, in which the mass variable is specified at each cell center and the *normal* velocity component is specified at each edge, are popular choices due to their ability to conserve global invariants (e.g. [3]) along with an accurate representation of the inertial-gravity modes, provided that the Rossby deformation radius is well resolved. However, if the Rossby deformation radius is not well resolved, which is the case in current global ocean general circulation models, the performance of the C-grid schemes is severely downgraded ([1, 2, 3]).

Various efforts have been undertaken to improve and/or extend the C-grid staggering technique. Lin and Rood ([13]) presents a splitting-step CD-grid scheme for the shallow water equations (SWE), in which, the prognostic variables evolve on the D-grid while the C-grid is used in the midpoint predictor step. But their scheme seems to inherit the poor C-grid response for the marginally resolved inertial modes and the poor D-grid response for the gravity modes ([18]). Adcroft et. al. ([1]) introduces a combination of the C- and D-grid schemes, also termed CD-grid, where the thickness variables are specified at the cell centers and both velocity components are specified on the edges. However, due to the imbalance between the number of degrees of freedom (n.d.f.) of the thickness and velocity variables, this scheme introduces computational modes that need to be filtered by an implicit time stepping technique. The TRiSK scheme of Thuburn et. al. ([21]) and Ringler et. al. [17] is based on a mapping that reconstructs the tangential velocity component at one cell edge from normal velocity components on neighboring cell edges. By design, TRiSK conserves mass up to round off errors. It also conserves PV and energy up to time truncation errors. However, TRiSK seems to be sensitive to the singularities in the global spheric grids and has trouble maintaining a consistent convergence rate at high resolutions ([17], [11]). Randall ([16]) proposes the Z-grid scheme that solves the SWE through

---

*Email address:* qchen@lanl.gov (Qingshan Chen)

its vorticity-divergence formulation. The scheme achieves the optimal representation of the inertial-gravity modes among the class of second-order accurate numerical schemes, and is free of the defects of the C-grid scheme when the Rossby deformation radius is not well resolved. But, having to globally invert two elliptic equations at each time step, the Z-grid scheme faces serious computational obstacles in long-term simulations of geophysical flows.

We endeavor to develop an alternative numerical scheme that mitigates the cost issue of the Z-grid scheme, maintains competitive dispersive relations on a wide range of wavenumber spaces, and is applicable on unstructured grids, including unstructured non-orthogonal grids. We take a co-volume strategy towards this goal. Without dwelling into technical details, we can explain this strategy as follows. Staggered grids, which comprise primary cells and dual cells, will be employed in the discretization. The dual cell centers are the vertices of the primary cells, and vice versa. The term “co-volume” comes from the fact that the SWE system evolves on both the primary cells and the dual cells. To make this possible, the thickness variable needs to be defined at both the primary cell centers and the dual cell centers, and both the normal and tangential velocity components need to be present on the edges. Due to its flux-form formulation, the scheme intrinsically conserves the mass. For the discretization of the Coriolis term, there is no reconstruction of the tangential velocity component involved because, at each edge, the velocity vector is completely represented by both of the velocity components. This discrete setup should also make the co-volume schemes flexible and robust. We draw this preliminary conclusion based on two observations. First, unlike the CD-grid scheme of [1], the n.d.f. of the thickness variable is now able to balance the n.d.f. of the velocity on arbitrary staggered grids, thanks to the additional and crucial presence of the discrete thickness variables on the dual cell centers. Second, the fact that both velocity components are natively specified on each edge makes it possible for the scheme to adapt to grids that are not orthogonal, i.e. the dual cell edges do not necessarily intersect the primary cell edges orthogonally. The last claim, if established, will render the co-volume schemes applicable on a much wider class of grids.

Similar techniques with the same name have been applied by Nicolaides et. al. to the curl-div systems in electromagnetics [15] and to incompressible flows [14], based on the curl-div formulation of the model, and by Baughman and Walkington [4] to the classical Stefan problem that models heat conduction in materials undergoing phase changes. The idea of introducing

extra degrees of freedom into the system in order to improve the dispersive relations has been employed by Xiao et. al. ([25]) to develop the collocated M-grid scheme. But the formulation of the M-grid scheme is fundamentally different from ours, and the two schemes also have different dispersive relations, as we shall see later.

In the rest of this article, we systematically and thoroughly explore the potential of our co-volume strategy in simulating geophysical flows. But first, in Section 2, we prototype the co-volume schemes for the Linear Shallow-Water Equations (LSWE) on a general orthogonal staggered grid. In Section 3, we perform linear wave analysis on the co-volume schemes on both the quadrilateral and the hexagon-triangular staggered grids in order to evaluate the method’s ability to simulate linear wave dynamics. In Section 4, we present the co-volume scheme for the Nonlinear Shallow-Water Equations (NSWE) on unstructured and non-orthogonal staggered grids; the scheme on orthogonal grids will then follow as a special case. Here we constrain modeling choices present in the scheme such that potential vorticity and total energy is conserved. Numerical results for the NSWE on Delaunay-Voronoi (orthogonal) grids are reported in Section 5. We conclude in Section 6.

## 2. A co-volume scheme for linearized shallow water equations on generic orthogonal staggered grids

### *Grid information and notations*

We consider a general orthogonal grid, on which the vertices of the primary mesh cells are the centers of the dual mesh cells, and vice versa. The dual cell edges intersect the primary cell edges orthogonally. An example of such a grid is shown in Fig. 2.1. The classification of general orthogonal grids covers many meshes currently used in climate modeling, such as latitude-longitude grids, Voronoi tessellations (aka “icosahedral grids”), Delaunay triangulations and conformally-mapped cubed sphere meshes.

In order to describe the co-volume discretization, some notations are needed. As shown in the diagram in Figure 2.2, the primary cells are indexed by  $i$ , and the dual cells by  $\nu$ . Hence the primary cells are referred to as  $A_i$ , and the dual cells as  $D_\nu$ . When no confusion should arise, we also use  $A_i$  and  $D_\nu$  to denote the areas of the primary and dual cells, respectively. Each primary cell edge corresponds to a unique and distinct dual cell edge,

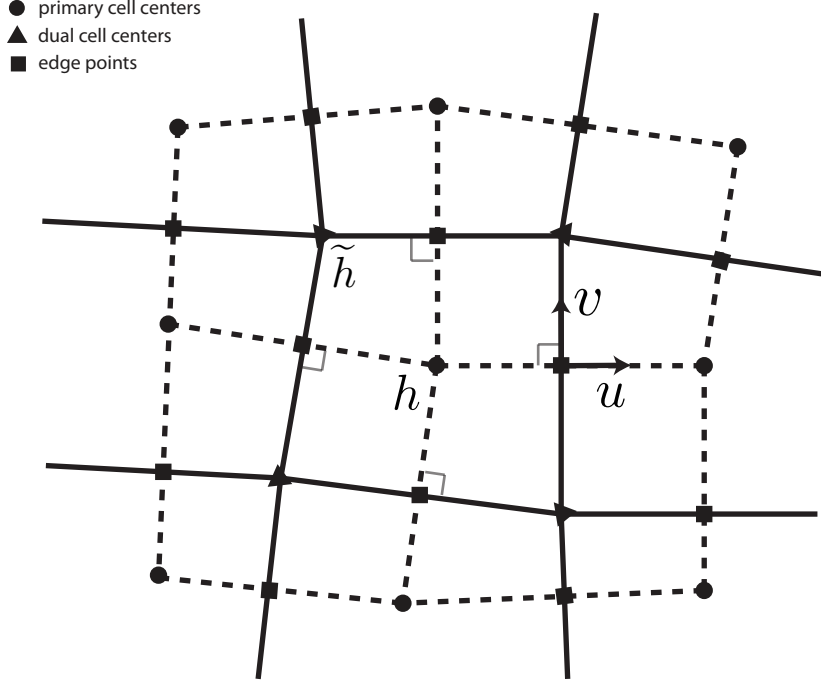


Figure 2.1: An example of a generic orthogonal staggered grid. The vertices of the primary mesh cells (solid line) are the centers of the dual mesh cells (dashed line), and vice versa. The dual cell edges intersect the primary cell edges orthogonally.

and such pairs of edges are indexed by  $e$ . Upon the edge pair  $e$ , the distance between the two neighboring primary cell centers is denoted as  $d_e$ , while the distance between the two neighboring dual cell centers is denoted as  $l_e$ . The connectivity information of the unstructured staggered grid is provided by six *sets of elements* defined in Table 1. For each edge  $e$ , a unit vector  $\mathbf{n}_e$  is defined to be orthogonal to the primary cell edge and therefore parallel to the dual cell edge. A second unit vector  $\mathbf{t}_e$  is defined as

$$\mathbf{t}_e = \mathbf{k} \times \mathbf{n}_e, \quad (2.1)$$

where  $\mathbf{k}$  denotes the vertical upward unit vector. Thus  $\mathbf{t}_e$  is orthogonal to the dual cell edge but parallel to the primary cell edge, and points to the vertex on the left side of  $\mathbf{n}_e$ . For each  $e$  and for each  $i \in \text{CE}(e)$ , i.e. the set of cells on edge  $e$  (see Table 1), we define the indicator

$$n_{e,i} = \begin{cases} 1 & \text{if } \mathbf{n}_e \text{ points away from primary cell } A_i, \\ -1 & \text{if } \mathbf{n}_e \text{ points towards primary cell } A_i, \end{cases} \quad (2.2)$$

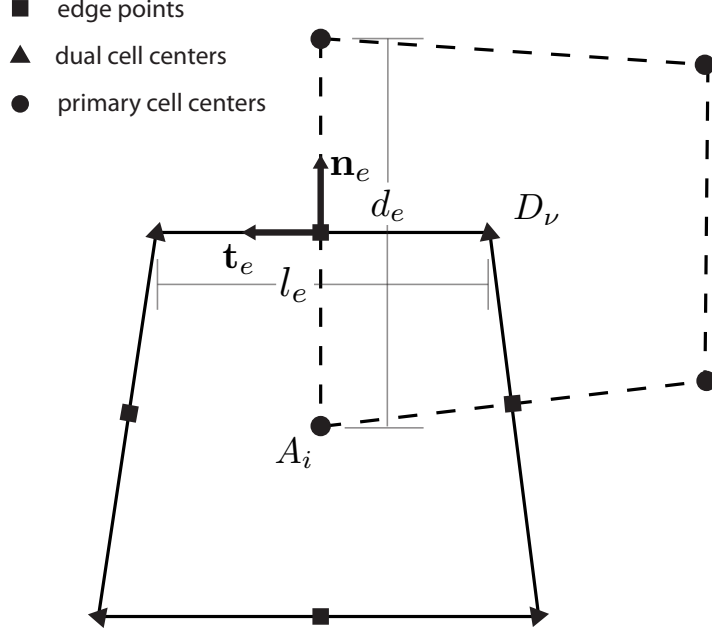


Figure 2.2: A diagram for a generic orthogonal staggered grid. The primary cells are indexed  $i$ , the dual cells by  $\nu$ , and the edges by  $e$ .

and for each  $\nu \in \text{VE}(e)$ ,

$$t_{e,\nu} = \begin{cases} 1 & \text{if } \mathbf{t}_e \text{ points away from dual cell } D_\nu, \\ -1 & \text{if } \mathbf{t}_e \text{ points towards dual cell } D_\nu. \end{cases} \quad (2.3)$$

The LSWEs are given by

$$\frac{\partial}{\partial t} h + H \nabla \cdot \mathbf{u} = 0, \quad (2.4)$$

$$\frac{\partial}{\partial t} \mathbf{u} + f \mathbf{k} \times \mathbf{u} = -g \nabla h, \quad (2.5)$$

where  $H$  is a constant scalar denoting the average fluid thickness,  $h$  a scalar denoting the small perturbation to the fluid thickness, and  $\mathbf{u}$  ( $\equiv (u, v)$  on a Cartesian coordinate) a vector denoting the perturbation to the velocity field of a fluid at still.

The thickness variables are placed at both the primary and the dual cell centers. The thickness variables at the primary cell centers are denoted as  $h_i$ ,

Table 1: Sets of elements defining the connectivity of a unstructured dual grid.

Set	Definition
$EC(i)$	Set of edges defining the boundary of primary cell $A_i$
$VC(i)$	Set of dual cells that form the vertices primary cell $A_i$
$CE(e)$	Set of primary cells boarding edge $e$
$VE(e)$	Set of dual cells boarding edge $e$
$CV(\nu)$	Set of primary cells that form vertices of dual cell $D_\nu$
$EV(\nu)$	Set of edges that define the boundary of dual cell $D_\nu$

and the thickness variable at the dual cell centers are denoted as  $\tilde{h}_\nu$ . On the primary cell edges, both the normal ( $u_e \mathbf{n}_e$ ) and the tangential ( $v_e \mathbf{t}_e$ ) velocity components are present. The same can be said of the dual cell edges, though the roles for  $u_e$  and  $v_e$  are swapped.

The co-volume scheme for the LSWEs (2.4)–(2.5) is then given by

$$\frac{\partial}{\partial t} h_i + H[\nabla \cdot \mathbf{u}]_i = 0, \quad (2.6)$$

$$\frac{\partial}{\partial t} \tilde{h}_\nu + H[\nabla \cdot \mathbf{u}]_\nu = 0, \quad (2.7)$$

$$\frac{\partial}{\partial t} u_e - f v_e = -g[\nabla h]_{e,n}, \quad (2.8)$$

$$\frac{\partial}{\partial t} v_e + f u_e = -g[\nabla h]_{e,t}. \quad (2.9)$$

The equations (2.6) and (2.7) result from the flux-form discretization of the thickness equation (2.4) on the primary and dual cells, respectively, whereas the equations (2.8) and (2.9) are obtained by projecting the momentum equation (2.5) in the directions of  $\mathbf{n}_e$  and  $\mathbf{t}_e$ , respectively. In the above, the discrete divergence operators  $[\nabla \cdot (\cdot)]_i$  on the primary cells and  $[\nabla \cdot (\cdot)]_\nu$  on the

dual cells, when applied on the velocity field  $\mathbf{u}$ , are defined as

$$[\nabla \cdot \mathbf{u}]_i = \frac{1}{A_i} \sum_{e \in EC(i)} u_e l_e n_{e,i}, \quad (2.10)$$

$$[\nabla \cdot \mathbf{u}]_\nu = \frac{1}{D_\nu} \sum_{e \in EV(\nu)} v_e d_e t_{e,\nu}, \quad (2.11)$$

respectively. The discrete gradient operator  $[\nabla(\cdot)]_{e,n}$  in the normal direction, and  $[\nabla(\cdot)]_{e,t}$  in the tangential direction, when applied to the thickness field, are defined as

$$[\nabla h]_{e,n} = \frac{-1}{d_e} \sum_{i \in CE(e)} h_i n_{e,i}, \quad (2.12)$$

$$[\nabla h]_{e,t} = \frac{-1}{l_e} \sum_{\nu \in VE(e)} \tilde{h}_\nu t_{e,\nu}, \quad (2.13)$$

respectively. If the primary cell edges and the dual cell edges intersect at the midpoints, then (2.12) and (2.13) are the second-order finite difference approximations to the gradient operator in normal and tangential directions, respectively.

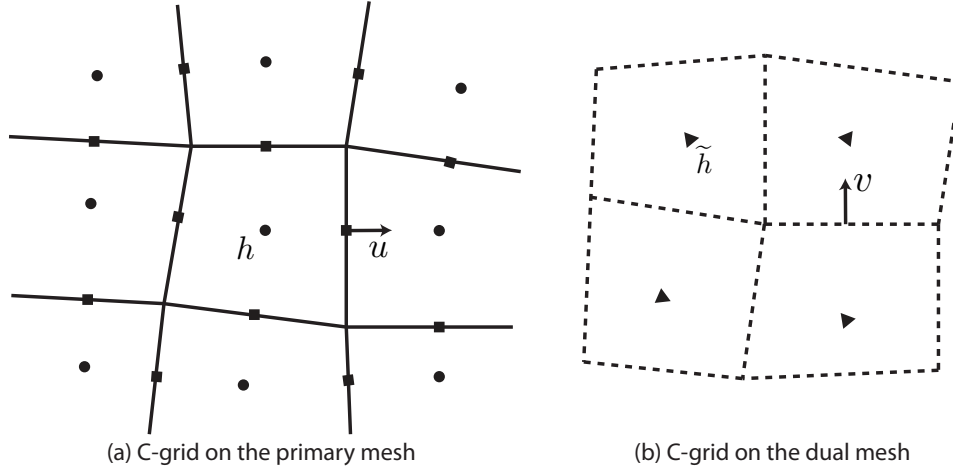


Figure 2.3: The co-volume scheme can be viewed as a C-grid scheme on the primary mesh coupled with a C-grid scheme on the dual mesh. (a) C-grid on the primary mesh; (b) C-grid on the dual mesh.



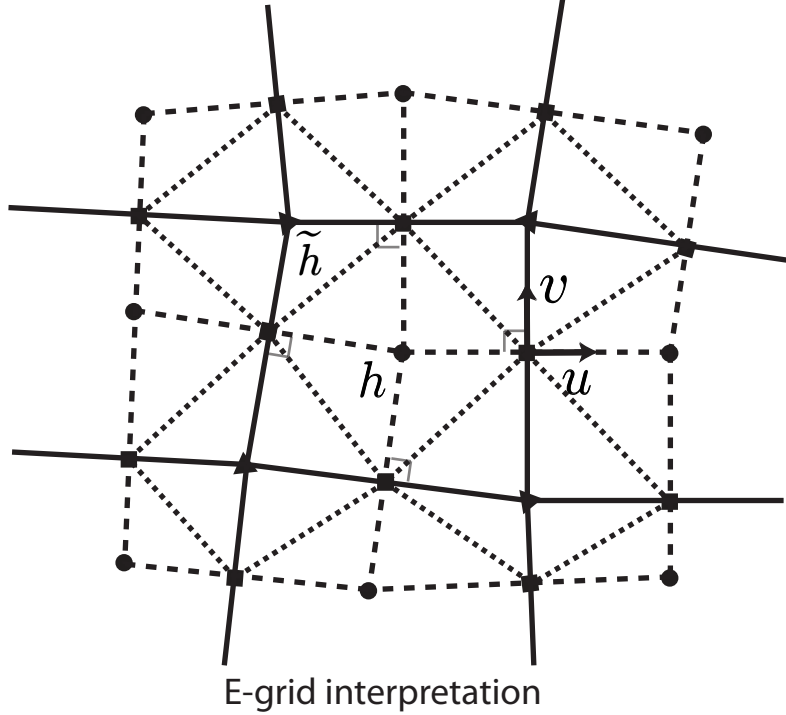


Figure 2.4: The co-volume scheme on the quadrilateral staggered grid (solid and dashed lines) can also be viewed as an E-grid scheme on the mesh (dotted lines) connecting the velocity points.

It is obvious that the co-volume scheme on an orthogonal staggered grid can be viewed as a C-grid scheme on the primary mesh coupled with a C-grid scheme on the dual mesh. In the case of LSWE, the coupling is through the Coriolis forcing solely. In Figure 2.3 the co-volume scheme on the generic orthogonal staggered grid of Figure 2.1 is decoupled into two C-grid schemes, one on the primary mesh and the other on the dual mesh. When the Coriolis parameter  $f$  vanishes, the two C-grid schemes on the primary and dual meshes are completely decoupled, and there is a concern that these two systems may drift far too apart. We will address this issue in Section 5.

The co-volume scheme can also be interpreted as a generalization of the traditional E-grid scheme ([2]) onto unstructured grids. For example, on the staggered grid of Figure 2.1, if we connect all the velocity points around each primary cell center and all the velocity points around each dual cell center, then we have a non-overlapping tiling of the whole domain by quadrilaterals

(Figure 2.4). The thickness variables ( $h$  and  $\tilde{h}$ ) are defined at the quadrilateral cell centers and the velocity components are defined at the vertices, which is exactly how the variables are distributed in a E-grid scheme. In our generalized E-grid scheme, there are always four cells around each vertex away from the boundary, but the cells do not have to be quadrilaterals. For instance, the mesh connecting the velocity points on a hexagon-triangular staggered grid comprises of triangles and hexagons.

Now that the co-volume scheme can be interpreted either as coupled, overlapping C-grid schemes on the primary and dual meshes, or as a traditional, non-overlapping E-grid scheme, the question arises as how the dispersive relations obtained through these interpretations are related to each other. Also presented is the question about how to use the computational data for analysis and postprocessing. Using all of the data as they are associated with the E-grid is unlikely a good choice due to the well-known shortcomings of E-grid scheme ([2]). Assuming that the primary mesh mostly consists of hexagons, using only the data associated with the C-grid scheme on such a mesh seems an attractive option, given that the C-grid schemes enjoy satisfactory dispersive relations on hexagonal meshes ([20]). We will come back to these essential issues as we present results from the linear wave analysis and numerical experiments.

### 3. Dispersive wave analysis

Dispersive wave analysis is usually employed to evaluate how well a numerical scheme solve the dispersive wave modes in a linear system. In this section we carry out such analysis on the co-volume schemes for LSWE on the quadrilateral staggered grid and the hexagon-triangular staggered grid. Even though the co-volume scheme can be either viewed as two coupled C-grid schemes, or as a single E-grid scheme, we only carry out linear wave analysis from the first perspective, i.e. the C-grid variables on the primary mesh and on the dual mesh are treated separated. On a uniform quadrilateral staggered grid, the E-grid interpretation is associated with a new uniform quadrilateral mesh, on which the linear wave analysis of the E-grid is available in the literature ([2, 16]). On a hexagon-triangular staggered grid, the E-grid interpretation is associated with a new mesh that comprises of hexagons and triangles. Due to the non-uniformity in the cell shapes and resolutions of this mesh, a rigorous linear wave analysis of the E-grid scheme is not possible.

*The continuous case*

Substituting a wave-form solution

$$\begin{pmatrix} h \\ u \\ v \end{pmatrix} = \begin{pmatrix} \Phi \\ U \\ V \end{pmatrix} e^{i(kx+ly-\omega t)} \quad (3.1)$$

into (2.4)–(2.5), we easily find the dispersion relations between the wave numbers in the  $x$ -,  $y$ - and the temporal directions, namely,

$$\omega = 0, \quad (3.2)$$

$$\omega^2 = f^2 + gH(k^2 + l^2). \quad (3.3)$$

The first relation (3.2) represents the stationary geostrophic modes of the flow, whereas (3.3) represents the inertial-gravity modes. It is customary to normalize  $\omega$  by  $f$ , and by doing so, we obtain from (3.2) that

$$\left(\frac{\omega}{f}\right)^2 = 1 + R^2 (k^2 + l^2), \quad (3.4)$$

where  $R = \sqrt{gH}/f$  denotes the Rossby deformation radius.

*The quadrilateral case*

The variables are distributed as described in the previous section, and also see Figure 3.1. The co-volume scheme on the uniform quadrilateral staggered grid can be viewed as the E-grid scheme on a uniform quadrilateral mesh connecting the velocity points, just as discussed in the previous section. It is well-known that, when the grid collapses in one direction (along the horizontal or vertical direction in our case), the E-grid scheme becomes an one-dimensional A-grid, and thus inherits all the shortcomings of the latter. Here, we first adopt the other view of the co-volume scheme as coupled C-grid schemes on the primary and dual meshes, and analytically derive the dispersive relations for the corresponding C-grid variables. Then we come back to discuss how these results relate to the interpretation of the co-volume scheme as an E-grid scheme.

For the purpose of the linear wave analysis on this particular grid, we further adopt the following naming conventions. We refer to the normal velocity components (w.r.t. the primary cells) that point to the right as  $u^1$ , the normal velocity components that point up as  $u^2$ , the tangential velocity

components (w.r.t. the primary cells) that point up as  $v^1$ , and the tangential velocity components that point to the left as  $v^2$ . The primary cells (solid line) are indexed by  $(m, n)$ , with  $m$  and  $n$  running over all the integers. The dual cells (dashed line) are then indexed by  $(m + 1/2, n + 1/2)$ , and the edges by  $(m, n + 1/2)$  or  $(m + 1/2, n)$ . The distance between two adjacent primary cell centers is denoted by  $d$  (Figure 3.1). The normal unit vectors (w.r.t. the primary cells) point either to the right or upwards, and the tangential unit vectors (also w.r.t. the primary cells) point either upwards or to the left, thus conforming to the definition (2.1).

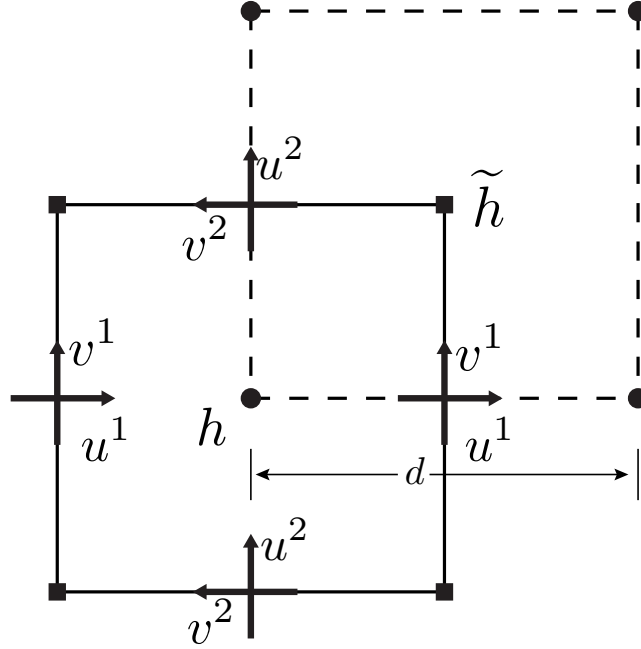


Figure 3.1: A uniform quadrilateral staggered grid. Thickness ‘lives’ at both the primary cell (solid line) centers and the dual cell (dashed line) centers. On each edge, both velocity components are present.

With these notations for the quadrilateral grid, the co-volume (2.6) – (2.9)

then takes the following form:

$$\left\{ \begin{array}{l} \frac{\partial}{\partial t} h_{m,n} + \frac{H}{d} \left( u_{m+\frac{1}{2},n}^1 - u_{m-\frac{1}{2},n}^1 + u_{m,n+\frac{1}{2}}^2 - u_{m,n-\frac{1}{2}}^2 \right) = 0, \\ \frac{\partial}{\partial t} \tilde{h}_{m+\frac{1}{2},n+\frac{1}{2}} + \frac{H}{d} \left( -v_{m+1,n+\frac{1}{2}}^2 \right. \\ \quad \left. + v_{m,n+\frac{1}{2}}^2 + v_{m+\frac{1}{2},n+1}^1 - v_{m+\frac{1}{2},n}^1 \right) = 0, \\ \frac{\partial}{\partial t} u_{m+\frac{1}{2},n}^1 - f v_{m+\frac{1}{2},n}^1 + \frac{g}{d} (h_{m+1,n} - h_{m,n}) = 0, \\ \frac{\partial}{\partial t} v_{m+\frac{1}{2},n}^1 + f u_{m+\frac{1}{2},n}^1 + \frac{g}{d} (\tilde{h}_{m+\frac{1}{2},n+\frac{1}{2}} - \tilde{h}_{m+\frac{1}{2},n-\frac{1}{2}}) = 0, \\ \frac{\partial}{\partial t} u_{m,n+\frac{1}{2}}^2 - f v_{m,n+\frac{1}{2}}^2 + \frac{g}{d} (h_{m,n+1} - h_{m,n}) = 0, \\ \frac{\partial}{\partial t} v_{m,n+\frac{1}{2}}^2 + f u_{m,n+\frac{1}{2}}^2 + \frac{g}{d} (\tilde{h}_{m-\frac{1}{2},n+\frac{1}{2}} - \tilde{h}_{m+\frac{1}{2},n+\frac{1}{2}}) = 0. \end{array} \right. \quad (3.5)$$

We note that,  $u^1$  and  $u^2$ , which are normal to the primary cells, defines the potential vorticity on the dual cells, and on the other hand,  $v^1$  and  $v^2$ , which are normal to the dual cells, defines the potential vorticity on the primary cells. This notion will play an essential role in extending the scheme to nonlinear shallow water equations in Section 4.

The dispersive relations between the discrete wave numbers in the  $x$ -,  $y$ - and the temporal directions are found by substituting the canonical wave form solutions

$$\begin{pmatrix} h \\ \tilde{h} \\ u^1 \\ u^2 \\ v^1 \\ v^2 \end{pmatrix} = \begin{pmatrix} \Phi \\ \tilde{\Phi} \\ U^1 \\ U^2 \\ V^1 \\ V^2 \end{pmatrix} e^{i(kmd+ln d-\omega t)} \quad (3.6)$$

into (3.5). A set of six equations results for the Fourier coefficients  $\Phi, \tilde{\Phi}, U^1, U^2, V^1, V^2$ , with expressions involving the discrete wave numbers as coefficients. For there to be non-trivial solutions for the Fourier coefficients, it must hold that the coefficient matrix has a non-empty null space, or equivalently, its determinant vanishes. Using the last condition, we solve for the

dispersive relation between the discrete wave numbers,

$$\omega = 0, \quad (\text{multiplicity } 2) \quad (3.7)$$

$$\omega^2 = f^2 + \frac{4gH}{d^2} \left( \sin^2 \frac{1}{2} kd + \sin^2 \frac{1}{2} ld \right). \quad (\text{multiplicity } 2) \quad (3.8)$$

The relation (3.8) can also be written as

$$\left( \frac{\omega}{f} \right)^2 = 1 + \frac{4R^2}{d^2} \left( \sin^2 \frac{1}{2} kd + \sin^2 \frac{1}{2} ld \right). \quad (3.9)$$

The dispersive relation (3.9) is formally identical to that for the Z-grid scheme (see Figure 1 in [16]). We should note this identification happens when the view of the co-volume scheme as couple C-grid schemes is taken. The relation between this dispersive relation and that obtained through the E-grid interpretation will be discussed later. The relation (3.9) shows that each set of the C-grid variables in the co-volume scheme resolves the inertial-gravity wave modes equally well as the Z-grid scheme. Plots of the dispersive relation of the Z-grid scheme can be found in the reference just cited and will not be reproduced here. But it is worth mentioning that, when the Rossby deformation radius is well resolved, the co-volume on either of the dual meshes on a uniform staggered quadrilateral grid, just like the Z-grid scheme, resolves the inertial-gravity waves slightly better than the classical C-grid scheme, and when the Rossby deformation radius is under resolved, still maintains a monotonically increasing dispersive relation. The co-volume scheme achieves this without the burden of globally inverting elliptic equations, but at the cost of evolving a double-sized system compared to the classical C-grid scheme. The dispersive relation of the M-grid scheme ([25]) is close to that of the Z-grid scheme when the Rossby deformation radius is well resolved, and appears slightly downgraded when the opposite is true, but the dimensionless ratio  $\omega/f$  remains above 1.

As mentioned earlier, when the co-volume scheme (or the E-grid interpretation of it) on uniform quadrilateral grids collapses in one direction, it becomes an A-grid scheme. The smallest wave length that it is capable of resolving is  $d$ , corresponding to a maximum wave number of  $2\pi/d$ . The wave along the collapsing direction has, of course, a wave number zero. Hence the whole space of resolved wave numbers on a uniform quadrilateral grid forms a right triangle ([2, 16]). The primary mesh alone, as well as the dual mesh,

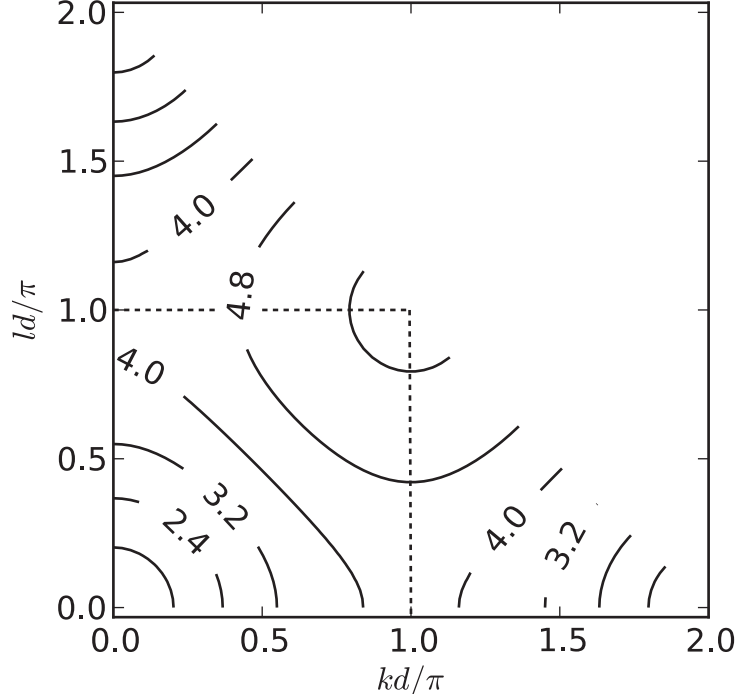


Figure 3.2: Inertial-gravity wave frequencies for the E-grid scheme.

on a quadrilateral staggered grid, can resolve wave lengths as short as  $2d$ , corresponding to a maximum wave number of  $\pi/d$ , in both the horizontal and vertical directions. Hence the primary mesh or the dual mesh alone resolves half of the wavenumber space that are resolved by the combined staggered grid. The dispersive relation of the E-grid scheme on this triangular wave number space can be found in the references just cited, and is reproduced in Figure 3 for the ratio  $R/d = 2$ . We point out that the contour plot in the sub-region bounded by the dotted lines for the wave numbers  $0 \leq kd/\pi \leq 1$  and  $0 \leq ld/\pi \leq 1$  exactly matches the dispersive relation (3.9) for the co-volume scheme on either of the dual meshes on the staggered uniform quadrilateral grid. Hence, by choosing the C-grid data on the primary or dual mesh at the post-processing stage, we effectively filter out the short waves with either  $k \geq \pi/d$ , or  $l \geq \pi/d$ . What are left constitute good approximation to the physical inertial gravity waves. Due to the isotropic nature of the uniform quadrilateral staggered grids, there is no difference between the primary mesh or the dual mesh. This is no longer true with the uniform hexagon-triangular

staggered grid, which we are going to discuss next.

### *The hexagon-triangular case*

A hexagon-triangular staggered grid is shown in Fig. 3.3. We refer to the hexagons as the primary cells, and the triangles as the dual cells. The normal unit vectors on the primary cell edges point to the right, the upper right or the lower right, depending on the edges they are associated with. The tangential unit vectors are determined according to (2.1). The distance between two neighboring primary cell centers is again denoted as  $d$ .

As explained at the beginning of this section, a rigorous linear wave analysis is not possible for the E-grid interpretation of the co-volume scheme because of the non-uniformity in the cell shapes and resolutions in the new mesh that the E-grid scheme is associated with. On the other hand, it is possible if the co-volume scheme is viewed as as coupled C-grid schemes on the hexagonal and triangular meshes. In what follows, we adopt this interpretation and carry out the linear wave analysis. This interpretation will not identify the entire wavenumber space resolved by the meshes, but in the process we discuss the implications of taking this interpretation.

As for the general orthogonal grid in Section 2 and the quadrilateral grid in the first half of this section, thickness variables are placed at both the primary and dual cell centers with the velocities on the edges. However, due to the multiple directions of symmetry inherent in the hexagonal cells and the inhomogeneity in the structure of the triangular grid, extra care needs to be taken in handling these discrete variables. As noted in the above, the normal unit vectors to the primary cells point in three directions. We distinguish the velocity component associated with these directions by superscripts <sup>1</sup>, <sup>2</sup> and <sup>3</sup> (see Fig. 3.3). The inherent inhomogeneity in the triangular grid is manifested by the fact that one set of triangles point upward and the rest point downward. These two sets of triangles form two distinct, uniform but non-orthogonal lattices, which mandates that they need to be treated separately in the linear wave analysis. We denote the thickness variables located at the centers of the upperward-pointing triangular cells as  $h^2$ , and those at the center of the downward-pointing triangular cells as  $h^3$ . The thickness variables at the primary cell centers are denoted as  $h^1$ . Thus we have nine prognostic variables:  $h^i$ ,  $u^i$ , and  $v^i$  for  $i = 1, 2, 3$ .

Due to the non-orthogonal directions inherent in the hexagonal (or triangular) mesh, it seems natural to work with a non-orthogonal coordinate



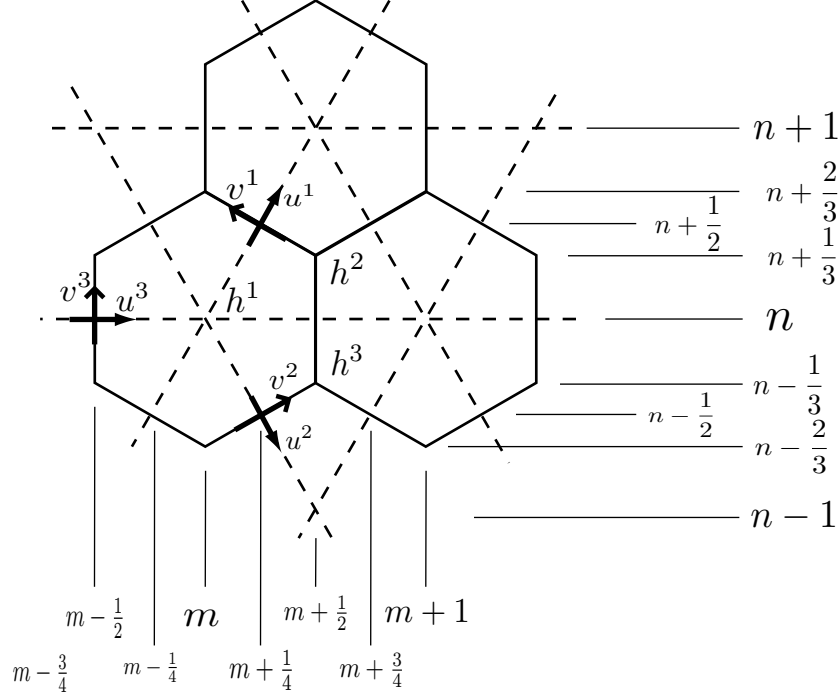


Figure 3.3: A uniform hexagon-triangular staggered grid. The horizontal positions are indexed by  $m$ , and the vertical positions by  $n$ . Each of the prognostic variables  $h^i$ ,  $u^i$  and  $v^i$ , for  $i = 1, 2, 3$ , resides on a uniform lattice.

system (see [20]), such as one with the two axes forming a  $60^\circ$  angle. However, placing the staggered hexagon-triangular grid on a classic Cartesian coordinate system has the advantage that the derived dispersive relations of the discrete system, yet to be presented, can then be compared to the familiar dispersive relations (3.2) and (3.3) of the continuous system on a Cartesian coordinate system. The dispersive relations on a non-orthogonal coordinate system generally involve cross products of wave numbers along each axis. Hence we choose to work with a Cartesian coordinate and number the y-axis positions of the grid points by  $n$ , and their x-axis positions by  $m$ ; see Fig. 3.3 for details.

With these proper notations for the hexagon-triangular grid, the co-

volume scheme (2.6)–(2.9) takes the following form:

$$\left\{ \begin{array}{l} \frac{dh_{m,n}^1}{dt} + \frac{\sqrt{3}Hd}{3A_{m,n}} \left( u_{m+\frac{1}{4},n+\frac{1}{2}}^1 - u_{m-\frac{1}{4},n+\frac{1}{2}}^2 - u_{m-\frac{1}{2},n}^3 \right. \\ \quad \left. - u_{m-\frac{1}{4},n-\frac{1}{2}}^1 + u_{m+\frac{1}{4},n-\frac{1}{2}}^2 + u_{m+\frac{1}{2},n}^3 \right) = 0, \\ \frac{dh_{m+\frac{1}{2},n+\frac{1}{3}}^2}{dt} + \frac{Hd}{D_{m+\frac{1}{2},n+\frac{1}{3}}} \left( v_{m+\frac{1}{4},n+\frac{1}{2}}^1 + v_{m+\frac{3}{4},n+\frac{1}{2}}^2 - v_{m+\frac{1}{2},n}^3 \right) = 0, \\ \frac{dh_{m+\frac{1}{2},n-\frac{1}{3}}^3}{dt} + \frac{Hd}{D_{m+\frac{1}{2},n-\frac{1}{3}}} \left( -v_{m+\frac{3}{4},n-\frac{1}{2}}^1 - v_{m+\frac{1}{4},n-\frac{1}{2}}^2 + v_{m+\frac{1}{2},n}^3 \right) = 0, \\ \frac{du_{m+\frac{1}{4},n+\frac{1}{2}}^1}{dt} - fv_{m+\frac{1}{4},n+\frac{1}{2}}^1 + \frac{g}{d} \left( h_{m+\frac{1}{2},n+1}^1 - h_{m,n}^1 \right) = 0, \\ \frac{dv_{m+\frac{1}{4},n+\frac{1}{2}}^1}{dt} + fu_{m+\frac{1}{4},n+\frac{1}{2}}^1 + \frac{\sqrt{3}g}{d} \left( h_{m,n+\frac{2}{3}}^3 - h_{m+\frac{1}{2},n+\frac{1}{3}}^2 \right) = 0, \\ \frac{du_{m+\frac{1}{4},n-\frac{1}{2}}^2}{dt} - fv_{m+\frac{1}{4},n-\frac{1}{2}}^2 + \frac{g}{d} \left( h_{m+\frac{1}{2},n-1}^1 - h_{m,n}^1 \right) = 0, \\ \frac{dv_{m+\frac{1}{4},n-\frac{1}{2}}^2}{dt} + fu_{m+\frac{1}{4},n-\frac{1}{2}}^2 + \frac{\sqrt{3}g}{d} \left( h_{m+\frac{1}{2},n-\frac{1}{3}}^3 - h_{m,n-\frac{2}{3}}^2 \right) = 0, \\ \frac{du_{m-\frac{1}{2},n}^3}{dt} - fv_{m-\frac{1}{2},n}^3 + \frac{g}{d} \left( h_{m,n}^1 - h_{m-1,n}^1 \right) = 0, \\ \frac{dv_{m-\frac{1}{2},n}^3}{dt} + fu_{m-\frac{1}{2},n}^3 + \frac{\sqrt{3}g}{d} \left( h_{m-\frac{1}{2},n+\frac{1}{3}}^2 - h_{m-\frac{1}{2},n-\frac{1}{3}}^3 \right) = 0. \end{array} \right. \quad (3.10)$$

In the above,  $A_{p,q}$  denotes the area of the primary cell that centers at  $(p, q)$ , and  $D_{p,q}$  the area of the dual cell that centers at  $(p, q)$ . The system (3.10) is complete with nine equations for nine prognostic variables  $h^i$ ,  $u^i$  and  $v^i$  for  $i = 1, 2, 3$ .

As before, we look for canonical wavelike solutions of (3.10), i.e. for  $i = 1, 2, 3$ , and for each proper index pair  $(p, q)$ ,

$$h_{p,q}^i = \Phi^i e^{i(kpd + \frac{\sqrt{3}}{2}lqd - \omega t)}, \quad (3.11)$$

$$u_{p,q}^i = U^i e^{i(kpd + \frac{\sqrt{3}}{2}lqd - \omega t)}, \quad (3.12)$$

$$v_{p,q}^i = V^i e^{i(kpd + \frac{\sqrt{3}}{2}lqd - \omega t)}. \quad (3.13)$$

Substituting (3.11)–(3.13) into (3.10) and eliminating the common factors from each equation result in a system of nine equations for the Fourier coefficients

$$(\Phi^1, \Phi^2, \Phi^3, U^1, U^2, U^3, V^1, V^2, V^3)^T.$$

The characteristic polynomial of this system, when solved for  $\omega$ , has the following roots:

$$\omega^3 = 0, \quad (3.14)$$

$$\omega^2 = f^2 + \frac{4gH}{3d^2} \left( 3 - \cos kd - 2 \cos \frac{1}{2}kd \cos \frac{\sqrt{3}}{2}ld \right), \quad (3.15)$$

$$\omega^2 = f^2 + \frac{4gH}{d^2} \left( 3 - \sqrt{3 + 2 \cos kd + 4 \cos \frac{1}{2}kd \cos \frac{\sqrt{3}}{2}ld} \right), \quad (3.16)$$

$$\omega^2 = f^2 + \frac{4gH}{d^2} \left( 3 + \sqrt{3 + 2 \cos kd + 4 \cos \frac{1}{2}kd \cos \frac{\sqrt{3}}{2}ld} \right). \quad (3.17)$$

Apparently, (3.14) represents the stationary geostrophic modes of the flow, some of which can be classified as *non-constant* pressure modes, with both velocity components being zero, the thickness variable on the primary mesh assuming a constant and the thickness variable on the dual mesh assuming a possibly different constant. We note that the classical C-grid scheme has *constant* pressure modes. To better expose the nature of the dispersive relations of (3.15)–(3.17), we resort to asymptotic analysis and find that, in the limit of  $d \rightarrow 0$ ,

$$\begin{aligned} 3 - \cos kd - 2 \cos \frac{1}{2}kd \cos \frac{\sqrt{3}}{2}ld &\sim \frac{3}{4}k^2d^2 + \frac{3}{4}l^2d^2, \\ \sqrt{3 + 2 \cos kd + 4 \cos \frac{1}{2}kd \cos \frac{\sqrt{3}}{2}ld} &\sim 3 - \frac{1}{4}k^2d^2 - \frac{1}{4}l^2d^2. \end{aligned}$$

Thus, both (3.15) and (3.16) represent the inertial-gravity modes of the flow,

because, in the limit  $d \rightarrow 0$ ,

$$\begin{aligned}\omega^2 &= f^2 + \frac{4gH}{3d^2} \left( 3 - \cos kd - 2 \cos \frac{1}{2}kd \cos \frac{\sqrt{3}}{2}ld \right) \\ &\sim f^2 + gH(k^2 + l^2),\end{aligned}$$

and

$$\begin{aligned}\omega^2 &= f^2 + \frac{4gH}{d^2} \left( 3 - \sqrt{3 + 2 \cos kd + 4 \cos \frac{1}{2}kd \cos \frac{\sqrt{3}}{2}ld} \right) \\ &\sim f^2 + gH(k^2 + l^2).\end{aligned}$$

Asymptotic analysis also shows that (3.17) represents grid-scale high-frequency computational modes, because

$$\begin{aligned}\omega^2 &= f^2 + \frac{4gH}{d^2} \left( 3 + \sqrt{3 + 2 \cos kd + 4 \cos \frac{1}{2}kd \cos \frac{\sqrt{3}}{2}ld} \right) \\ &\sim f^2 + \left( \frac{24}{d^2} - k^2 - l^2 \right) gH \\ &\geq f^2 + \frac{72 - 7\pi^2}{3d^2} gH \\ &> f^2.\end{aligned}$$

The last inequality is obtained when we take into consideration that  $0 \leq k \leq \pi/d$  and  $0 \leq l \leq 2\sqrt{3}\pi/3d$ . In this computational mode, the higher the spatial frequencies are, the lower the temporal frequency is; in other words, the slower the wave moves. For grid-scale oscillations, the temporal frequency reaches its minimum, which is still strictly larger than the planetary rotation frequency  $f$ . It is interesting to note that the CD-grid scheme of [1] and a majority of the finite element schemes analyzed in [12] admit a computational mode whose temporal frequency is exactly  $f$ , regardless of the spatial frequencies of the wave. We should also note that the grids used in their studies are different from ours.

It is known that triangular grids tend to produce spurious computational modes ([7]). Hence it is reasonable to suspect that the triangular mesh of the staggered grid is responsible for the computational modes of

(3.17). In order to verify this point, we artificially set  $f = 0$  in (3.10). Then the system for  $(\Phi^1, U^1, U^2, U^3)^T$  on the hexagonal grid and the system for  $(\Phi^2, \Phi^3, V^1, V^2, V^3)^T$  on the triangular grid completely decouple. The characteristic polynomial of the system for  $(\Phi^1, U^1, U^2, U^3)^T$ , when solved for  $\omega$ , has four roots:

$$\omega^2 = 0, \quad (3.18)$$

$$\omega^2 = \frac{4gH}{3d^2} \left( 3 - \cos kd - 2 \cos \frac{1}{2}kd \cos \frac{\sqrt{3}}{2}ld \right). \quad (3.19)$$

We note that (3.19) matches the gravity-wave part of (3.15), which indicates that the hexagonal grid is responsible for the inertial-gravity wave modes of (3.15) for the discrete system (3.10). It is also clear from (3.18) that the hexagonal grid is responsible for two of the three stationary geostrophic modes of (3.14). The characteristic polynomial of the system for  $(\Phi^2, \Phi^3, V^1, V^2, V^3)^T$  has five roots:

$$\omega = 0, \quad (3.20)$$

$$\omega^2 = \frac{4gH}{d^2} \left( 3 - \sqrt{3 + 2 \cos kd + 4 \cos \frac{1}{2}kd \cos \frac{\sqrt{3}}{2}ld} \right), \quad (3.21)$$

$$\omega^2 = \frac{4gH}{d^2} \left( 3 + \sqrt{3 + 2 \cos kd + 4 \cos \frac{1}{2}kd \cos \frac{\sqrt{3}}{2}ld} \right). \quad (3.22)$$

We readily notice that (3.21) matches the gravity-wave part of (3.16) and (3.22) matches the gravity-wave part of (3.17). This confirms that the triangular grid is responsible for the computational modes of (3.17), and the inertial-gravity wave modes of (3.16). It is also clear from (3.20) that the triangular grid is responsible for one of the three stationary modes of (3.14).

The E-grid interpretation of the co-volume scheme on a uniform hexagon-triangular grid involves a non-overlapping tiling of the plane by hexagons and triangles, which makes a rigorous dispersive wave analysis impossible. On the other hand, linear wave analysis on the coupled C-grid schemes clearly shows that the hexagonal mesh supports two steady mode and two inertial gravity modes, while the triangular mesh supports one steady modes, two inertial gravity modes, and two spurious modes. Thus, in a linearized system at least, choosing C-grid variables on the hexagonal mesh for post facto analysis and

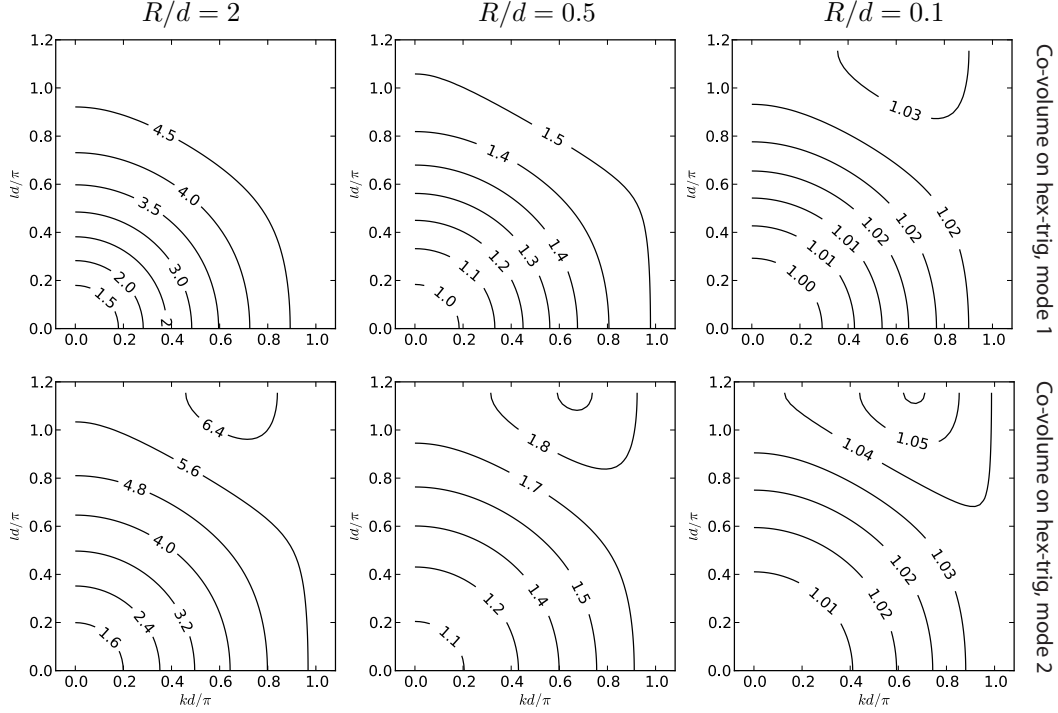


Figure 3.4: Inertial-gravity wave frequencies for the continuous system, the C-grid, D-grid and co-volume schemes, with  $R/d = 2$ . The co-volume outperforms the C-grid scheme in that its dispersive relations are closer to those of the continuous case. The CD-grid scheme of [1] and the Z-grid scheme possess the same inertial-gravity dispersive relations as the co-volume scheme.

post-processing will in effect discard the spurious modes, at the cost of the loss of the high quality steady modes and inertial gravity modes that also live on the triangular mesh.

We have shown in the first half of this section that, in the co-volume scheme, the data on either the primary mesh or the dual mesh, which expand exactly half of the total wavenumber space resolved by the co-volume scheme, has better representation of the inertial-gravity waves than the classical C-grid scheme when the Rossby deformation radius is well resolved, and they are free of the defects that the C-grid scheme has when the Rossby deformation radius is under-resolved. So far the linear wave analysis on the hexagon-triangular staggered grids only shows that the hexagonal mesh and the triangular mesh each supports an inertial-gravity wave mode in the limit of infinite fine resolution ( $d \rightarrow 0$ ). It is natural to ask how good these

approximate dispersive relations are when the resolutions are finite, and how they behave when the Rossby deformation radius is under-resolved. In Figure 3 we plot the dispersive relations (3.15) and (3.16), called “mode 1” and “mode 2”, respectively, for  $0 \leq k \leq \pi/d$ ,  $0 \leq l \leq 2\sqrt{3}\pi/3d$ , and for the ratios  $R/d = 2, 0.5, 0.1$ . The vertical wave number  $l$  has a wider range because the hexagonal mesh has a resolution  $\sqrt{3}d/2$  instead of  $d$  in the vertical direction. The triangular mesh potentially has more resolving power than the hexagonal mesh and is capable of resolving waves of higher wave numbers in both the horizontal and vertical directions, but this is complicated and we will only focus on the same range of wave numbers as for the hexagonal mesh. For all of the three  $R/d$  ratios studied, the dispersive relation (3.15) remains monotonically increasing in both  $k$  and  $l$ . The dispersive relation (3.16) remain positive everywhere and are largely monotonic, the only exceptions being where  $l$  is large (approximately when  $ld/\pi > 0.7$ ). In the regime where the Rossby deformation radius is well resolved, the dispersive relation (3.15) is slightly weaker than that of the C-grid scheme in the sense that it has a smaller maximum value for  $\omega$  in the resolved wave number range. On the other hand, the relation (3.16) shows a stronger performance with a larger maximum value, thanks to the additional but un-accounted resolving power on the triangular mesh. At  $R/d = 0.5$  the dispersive relation (3.16) remains very competitive, and the relation (3.15) starts to outperform the dispersive relation of the classical C-grid scheme. At  $R/d = 0.1$ , both relations (3.15) and (3.16) remain positive and largely monotonic, which demonstrates the robustness of the co-volume scheme on the hexagonal-triangular staggered grids. We note again that Figure 3 does not represent the whole wavenumber space resolved on the hexagon-triangular grid. The dispersive relation will unlikely remain monotone in the missing wavenumber space if it is known to us.

#### 4. A co-volume scheme for the nonlinear shallow water equations on generic non-orthogonal staggered grids

In this Section we present and study a co-volume scheme for the NSW on generic non-orthogonal staggered grids. The co-volume scheme on orthogonal staggered grids will follow as a special case.

The search for numerical schemes that can generalize to non-orthogonal staggered grids is motivated by the fact that defects are generally unavoidable

on grids over complex domains, e.g. the line between two neighboring cell centers is orthogonal to, but not intersecting the edge between them. Even in cases where it is possible to generate defect-free staggered grids, the cost of achieving them may be a concern, especially when adaptive mesh refinement (AMR) techniques are being applied. The scheme we are about to present is applicable to arbitrary conforming staggered grids. We also note that whether a dual cell edge intersects a primary cell edge has impact on the accuracy, but not on the applicability of the scheme.

The full nonlinear shallow water equations (NSWE), in the vector-invariant form, are given by

$$\begin{cases} \frac{\partial h}{\partial t} + \nabla \cdot (h\mathbf{u}) = 0, \\ \frac{\partial \mathbf{u}}{\partial t} + q\mathbf{k} \times h\mathbf{u} = -\nabla(gh + K), \end{cases} \quad (4.1)$$

where  $h$ ,  $\mathbf{u}$  denote the fluid thickness and horizontal velocity, respectively,  $q = (\mathbf{k} \cdot \nabla \times \mathbf{u} + f)/h$  the potential vorticity, and  $K = |\mathbf{u}|^2/2$  the per-unit-volume kinetic energy.

In Fig. 4.1 a generic non-orthogonal staggered grid is shown. The same notations from the Section 2 for generic orthogonal grids will be followed here, except for the changes/additions noted below. The unit vector  $\mathbf{n}_e$  is now defined to be along the dual cell edge, and is not necessarily normal to the primary cell edge on which it is located. The normal unit vector, which points in the same cell-to-cell direction as  $\mathbf{n}_e$ , is instead denoted as  $\hat{\mathbf{n}}_e$ . The tangential unit vector  $\mathbf{t}_e$  along the primary cell edge is defined as pointing to the vertex on the left-hand side of  $\mathbf{n}_e$ , or equivalently,

$$\mathbf{t}_e = \mathbf{k} \times \hat{\mathbf{n}}_e. \quad (4.2)$$

The unit vector normal to the dual cells and pointing in the same vertex-to-vertex direction as  $\mathbf{t}_e$  is denoted as  $\hat{\mathbf{t}}_e$ , and it is related to  $\mathbf{n}_e$  by

$$\hat{\mathbf{t}}_e = \mathbf{k} \times \mathbf{n}_e. \quad (4.3)$$

The unit vectors  $\mathbf{n}_e$  and  $\mathbf{t}_e$  form an angle  $\theta_e$ , which can be any value non-inclusively between  $0^\circ$  and  $180^\circ$ .

The discrete prognostic variables, i.e. the thickness and velocities, are distributed in exactly the same manner as in the case of LSWE on orthogonal staggered grids (see Section 2). The notations are also adopted, i.e. the



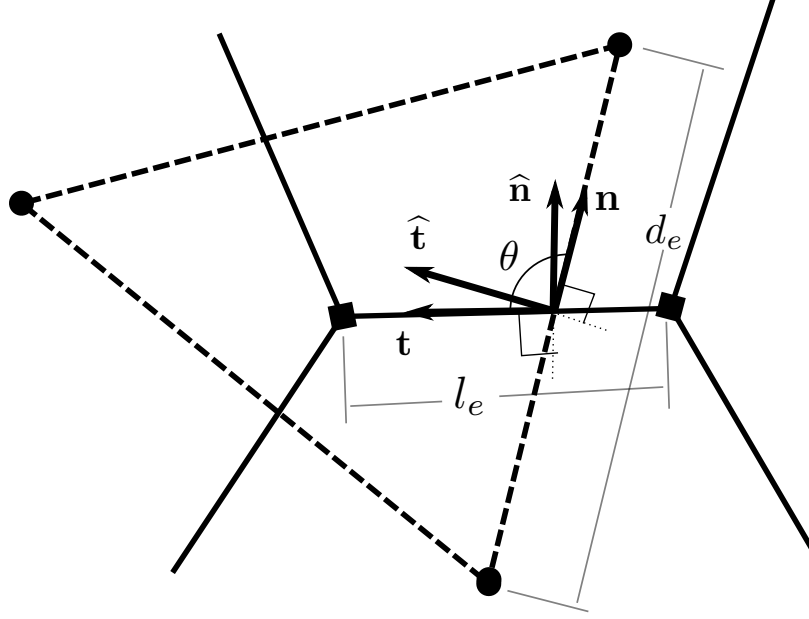


Figure 4.1: A generic non-orthogonal staggered grid. The primary cells are formed by solid lines, and the dual cells are formed by dashed lines.

thickness variables at primary cell centers are called  $h_i$ , the thickness variables at dual cell centers are called  $\tilde{h}_i$ , etc. However, due to the nonlinear nature of the system, new diagnostic variables are also needed. These diagnostic variables are defined below such that global system invariants are maintained.

On a two-dimensional domain, every set of two independent vectors form a complete coordinate system, and so do  $\mathbf{n}_e$  and  $\mathbf{t}_e$  for each  $e$ . The decomposition of an arbitrary velocity vector  $\mathbf{u}_e$  can be written as

$$\mathbf{u}_e = u_e \mathbf{n}_e + v_e \mathbf{t}_e. \quad (4.4)$$

The following scalar quantities can be easily calculated:

$$\mathbf{u}_e \cdot \mathbf{n}_e = u_e + v_e \cos \theta_e, \quad (4.5)$$

$$\mathbf{u}_e \cdot \mathbf{t}_e = u_e \cos \theta_e + v_e, \quad (4.6)$$

$$\mathbf{u}_e \cdot \hat{\mathbf{n}}_e = u_e \sin \theta_e, \quad (4.7)$$

$$\mathbf{u}_e \cdot \hat{\mathbf{t}}_e = v_e \sin \theta_e, \quad (4.8)$$

where, as we recall,  $\theta_e$  denotes the angle between  $\mathbf{n}_e$  and  $\mathbf{t}_e$ . Using the Stokes formula and (4.7), the thickness equation on the primary cell can be discretized as

$$\frac{dh_i}{dt} + \frac{1}{A_i} \sum_{e \in EC(i)} \bar{h}_e u_e l_e \sin \theta_e n_{e,i} = 0 \quad (4.9)$$

Similarly on the dual cell  $\nu$ ,

$$\frac{d\tilde{h}_\nu}{dt} + \frac{1}{D_\nu} \sum_{e \in EV(\nu)} \bar{h}_e v_e d_e \sin \theta_e t_{e,\nu} = 0, \quad (4.10)$$

Projecting (4.1)<sub>2</sub> in the direction of  $\mathbf{n}_e$  and using (4.2) and (4.5), we obtain

$$\frac{\partial}{\partial t}(u_e + v_e \cos \theta_e) - \bar{q}_e \bar{h}_e \mathbf{u}_e \cdot \hat{\mathbf{t}}_e = -\frac{\partial}{\partial \mathbf{n}_e}(gh + K). \quad (4.11)$$

Using (4.8) and a finite difference approximation for the right-hand side yields

$$\frac{\partial}{\partial t}(u_e + v_e \cos \theta_e) - \bar{q}_e \bar{h}_e v_e \sin \theta_e = \frac{1}{d_e} \sum_{i \in CE(e)} (gh_i + K_i) n_{e,i}. \quad (4.12)$$

In the above,  $\bar{h}_e$  denotes the fluid thickness on edges,  $\bar{q}_e$  the potential vorticity on edges, and  $K_i$  the kinetic energy on the primary cell centers. Similarly, in the direction of  $\mathbf{t}_e$ , a finite difference approximation to (4.1)<sub>2</sub> is obtained:

$$\frac{d}{dt}(u_e \cos \theta_e + v_e) + \bar{q}_e \bar{h}_e u_e \sin \theta_e = \frac{1}{l_e} \sum_{\nu \in VE(e)} (g\tilde{h}_\nu + K_\nu) t_{e,\nu}, \quad (4.13)$$

where  $K_\nu$  denotes the kinetic energy on the dual cell centers.

The co-volume scheme for the NSW (4.1) on a non-orthogonal grid consists of equations (4.9), (4.10), (4.12) and (4.13). The specification of the diagnostic variables  $K_i$ ,  $K_\nu$ ,  $\bar{q}_e$  and  $\bar{h}_e$  will be determined through the potential vorticity dynamical analysis and the energetic analysis of this discrete system.

#### *PV dynamics*

As usual, we denote the relative vorticity by  $\zeta$ , which is defined as

$$\zeta = \text{curl } \mathbf{u}. \quad (4.14)$$

Applying the Stokes formula on a dual cell  $D_\nu$ , we obtain

$$\int_{D_\nu} \zeta = \int_{D_\nu} \text{curl } \mathbf{u} = \int_{\partial D_\nu} \mathbf{u} \cdot \boldsymbol{\tau}, \quad (4.15)$$

where  $\boldsymbol{\tau}$  denotes the tangential vector along the edge of  $D_\nu$ . The relation (4.15) suggests a definition for the discrete curl operator on the dual cell  $D_\nu$ :

$$\tilde{\zeta}_\nu = \frac{-1}{D_\nu} \sum_{e \in EV(\nu)} (u_e + v_e \cos \theta_e) d_e t_{e,\nu}. \quad (4.16)$$

Similarly, on a primary cell  $A_i$ , the discrete curl operator can be defined as

$$\zeta_i = \frac{1}{A_i} \sum_{e \in EC(i)} (u_e \cos \theta_e + v_e) l_e n_{e,i}. \quad (4.17)$$

We apply the discrete curl operator (4.16) to equations (4.12) to obtain

$$\frac{d}{dt} \tilde{\zeta}_\nu + \frac{1}{D_\nu} \sum_{e \in EV(\nu)} \bar{q}_e \bar{h}_e v_e \sin \theta_e d_e t_{e,\nu} = \frac{1}{D_\nu} \sum_{e \in EV(\nu)} \sum_{i \in CE(e)} (gh_i + K_i) n_{e,i} t_{e,\nu}. \quad (4.18)$$

We note that the right-hand side of (4.18) is the discrete form of  $\nabla \times \nabla$ , and it vanishes (see [17] for a proof). We define the absolute vorticity and the potential vorticity on dual cell centers as

$$\tilde{\eta}_\nu = \tilde{\zeta}_\nu + \tilde{f}_\nu \quad \text{and} \quad \tilde{q}_\nu = \frac{\tilde{\eta}_\nu}{\tilde{h}_\nu}, \quad (4.19)$$

respectively. Then we derive from (4.18) that

$$\frac{d}{dt} (\tilde{q}_\nu \tilde{h}_\nu) + \frac{1}{D_\nu} \sum_{e \in EV(\nu)} \bar{q}_e \bar{h}_e v_e \sin \theta_e d_e t_{e,\nu} = 0, \quad (4.20)$$

which is the flux-form discretization of the thickness-weighted potential vorticity equation on the dual cells. Following a similar procedure, we define the absolute vorticity and the potential vorticity on the primary cell centers as

$$\eta_i = \zeta_i + f_i \quad \text{and} \quad q_i = \frac{\eta_i}{h_i}, \quad (4.21)$$

respectively. We then derive from the other discrete momentum equation (4.13) that

$$\frac{d}{dt}(q_i h_i) + \frac{1}{A_i} \sum_{e \in EC(i)} \bar{q}_e \bar{h}_e u_e \sin \theta_e l_e n_{e,i} = 0, \quad (4.22)$$

which is a flux-form discretization of the thickness-weighted PV equation on the primary cells. Choice has not been made with regard to  $\bar{q}_e$ , the potential vorticity on the edges. However, we can conclude that, with a proper definition for  $\bar{q}_e$ , the discretizations (4.43)<sub>3,4</sub> of the momentum equations preserve the PV dynamics up to time truncation errors. For  $\bar{q}_e$ , we choose

$$\bar{q}_e = \frac{1}{4} \left( \sum_{i \in CE(e)} q_i + \sum_{\nu \in VE(e)} \tilde{q}_\nu \right). \quad (4.23)$$

Taking PV on the edge as the average of the PV on the neighboring primary and dual cells serves to couple together the two subsystems on the primary and dual meshes.

#### *Energy conservation*

The per-unit-volume kinetic energy is given by

$$K = \frac{1}{2} |\mathbf{u}|^2 = \frac{1}{2} u^2 + \frac{1}{2} v^2 + uv \cos \theta. \quad (4.24)$$

Hence a consistent approximation of the kinetic energy on edge  $e$  is

$$\bar{K}_e = \frac{1}{2} u_e^2 + \frac{1}{2} v_e^2 + u_e v_e \cos \theta_e. \quad (4.25)$$

We multiply (4.12) by  $\bar{h}_e u_e$  and (4.13) by  $\bar{h}_e v_e$  to obtain

$$\bar{h}_e \frac{d}{dt} \frac{u_e^2}{2} + \bar{h}_e u_e \frac{d}{dt} (v_e \cos \theta_e) - \bar{q}_e \bar{h}_e^2 u_e v_e \sin \theta_e = \frac{\bar{h}_e u_e}{d_e} \sum_{i \in CE(e)} (gh_i + K_i) n_{e,i}, \quad (4.26)$$

$$\bar{h}_e \frac{d}{dt} \frac{v_e^2}{2} + \bar{h}_e v_e \frac{d}{dt} (u_e \cos \theta_e) + \bar{q}_e \bar{h}_e^2 u_e v_e \sin \theta_e = \frac{\bar{h}_e v_e}{l_e} \sum_{\nu \in VE(e)} (\tilde{g} h_\nu + K_\nu) t_{e,\nu} \dots \quad (4.27)$$

Combining (4.26) and (4.27) and also using (4.25), we find that

$$\begin{aligned} \frac{d}{dt}(\bar{h}_e \bar{K}_e) &= \bar{K}_e \frac{d}{dt} \bar{h}_e + \\ &\quad \frac{\bar{h}_e u_e}{d_e} \sum_{i \in CE(e)} (gh_i + K_i) n_{e,i} + \frac{\bar{h}_e v_e}{l_e} \sum_{\nu \in VE(e)} (g\tilde{h}_\nu + K_\nu) t_{e,\nu}. \end{aligned} \quad (4.28)$$

We define

$$\bar{A}_e = \frac{1}{2} d_e l_e \sin \theta_e. \quad (4.29)$$

Multiplying (4.28) by  $\bar{A}_e$  and summing over all edges, we have

$$\begin{aligned} \frac{d}{dt} \sum_e \bar{A}_e \bar{h}_e \bar{K}_e &= \sum_e \bar{A}_e \bar{K}_e \frac{d}{dt} \bar{h}_e + \sum_e \frac{\bar{h}_e u_e l_e \sin \theta_e}{2} \sum_{i \in CE(e)} (gh_i + K_i) n_{e,i} \\ &\quad + \sum_e \frac{\bar{h}_e v_e d_e \sin \theta_e}{2} \sum_{\nu \in VE(e)} (g\tilde{h}_\nu + K_\nu) t_{e,\nu} \end{aligned} \quad (4.30)$$

By exchanging the summation order over  $(e, i)$  and over  $(e, \nu)$ , we obtain

$$\begin{aligned} \frac{d}{dt} \sum_e \bar{A}_e \bar{h}_e \bar{K}_e &= \sum_e \bar{A}_e \bar{K}_e \frac{d}{dt} \bar{h}_e + \frac{1}{2} \sum_i (K_i + gh_i) \sum_{e \in EC(i)} \bar{h}_e u_e l_e \sin \theta_e n_{e,i} \\ &\quad + \frac{1}{2} \sum_\nu (K_\nu + g\tilde{h}_\nu) \sum_{e \in EV(\nu)} \bar{h}_e v_e d_e \sin \theta_e t_{e,\nu} \end{aligned} \quad (4.31)$$

The terms involving  $gh_i$  or  $g\tilde{h}_\nu$  represent the conversion between kinetic energy (KE) and potential energy (PE). We multiply (4.9) by  $A_i gh_i$ , and sum over all primary cells to obtain

$$\frac{d}{dt} \sum_i \frac{1}{2} A_i gh_i^2 = - \sum_i gh_i \sum_{e \in EC(i)} \bar{h}_e u_e l_e \sin \theta_e n_{e,i}. \quad (4.32)$$

Similarly with (4.10), we obtain

$$\frac{d}{dt} \sum_\nu \frac{1}{2} D_\nu g\tilde{h}_\nu^2 = - \sum_\nu g\tilde{h}_\nu \sum_{e \in EV(\nu)} \bar{h}_e v_e d_e \sin \theta_e t_{e,\nu}. \quad (4.33)$$

We define

$$KE = \sum_e \bar{A}_e \bar{h}_e \bar{K}_e, \quad (\text{Kinetic energy}) \quad (4.34)$$

$$PE_C = \sum_i \frac{1}{2} A_i g h_i^2, \quad (\text{Potential energy on primary cells}) \quad (4.35)$$

$$PE_V = \sum_\nu \frac{1}{2} D_\nu g \tilde{h}_\nu^2. \quad (\text{Potential energy on dual cells}) \quad (4.36)$$

Using these notations, we can write the sum of (4.30),  $\frac{1}{2} \times$  (4.32) and  $\frac{1}{2} \times$  (4.33) as

$$\begin{aligned} \frac{d}{dt} \left( KE + \frac{1}{2} PE_C + \frac{1}{2} PE_V \right) &= \sum_e \bar{A}_e \bar{K}_e \frac{d}{dt} \bar{h}_e + \\ &\frac{1}{2} \sum_i K_i \sum_{e \in EC(i)} \bar{h}_e u_e l_e \sin \theta_e n_{e,i} + \frac{1}{2} \sum_\nu K_\nu \sum_{e \in EV(\nu)} \bar{h}_e v_e d_e \sin \theta_e t_{e,\nu}. \end{aligned} \quad (4.37)$$

The PE/KE conversion terms from (4.31), (4.32) and (4.33) have canceled.

For energy conservation, we want the right-hand side of (4.37) to vanish, that is,

$$\begin{aligned} \sum_e \bar{A}_e \bar{K}_e \frac{d}{dt} \bar{h}_e + \frac{1}{2} \sum_i K_i \sum_{e \in EC(i)} \bar{h}_e u_e l_e \sin \theta_e n_{e,i} \\ + \frac{1}{2} \sum_\nu K_\nu \sum_{e \in EV(\nu)} \bar{h}_e v_e d_e \sin \theta_e t_{e,\nu} = 0. \end{aligned} \quad (4.38)$$

Using (4.9) and (4.10), we find (4.38) to be equivalent to

$$\sum_e \bar{A}_e \bar{K}_e \frac{d}{dt} \bar{h}_e - \sum_i \frac{A_i K_i}{2} \frac{d}{dt} h_i - \sum_\nu \frac{D_\nu K_\nu}{2} \frac{d}{dt} \tilde{h}_\nu = 0. \quad (4.39)$$

We let  $\bar{h}_e$  to be given by

$$\bar{h}_e = \frac{1}{4} \left( \sum_{i \in CE(e)} h_i + \sum_{\nu \in VE(e)} \tilde{h}_\nu \right). \quad (4.40)$$

Substituting (4.40) into (4.39), we conclude that (4.39), and so does (4.38), holds if

$$K_i = \frac{1}{2A_i} \sum_{e \in EC(i)} \bar{A}_e \bar{K}_e, \quad (4.41)$$

$$K_\nu = \frac{1}{2D_\nu} \sum_{e \in EV(\nu)} \bar{A}_e \bar{K}_e. \quad (4.42)$$

*A co-volume scheme for the NSWSE on orthogonal staggered grids*

By take  $\theta_e = 90^\circ$  for each  $e$  in (4.9), (4.10), (4.12) and (4.13), we obtain a co-volume scheme for the NSWSE on orthogonal grids, and it is listed below reference:

$$\begin{cases} \frac{dh_i}{dt} + \frac{1}{A_i} \sum_{e \in EC(i)} \bar{h}_e u_e l_e n_{e,i} = 0, \\ \frac{d\tilde{h}_\nu}{dt} + \frac{1}{D_\nu} \sum_{e \in EV(\nu)} \bar{h}_e v_e d_e t_{e,\nu} = 0, \\ \frac{du_e}{dt} - \bar{q}_e \bar{h}_e v_e = \frac{1}{d_e} \sum_{i \in CE(e)} (gh_i + K_i) n_{e,i}, \\ \frac{dv_e}{dt} + \bar{q}_e \bar{h}_e u_e = \frac{1}{l_e} \sum_{\nu \in VE(e)} (g\tilde{h}_\nu + K_\nu) t_{e,\nu}. \end{cases} \quad (4.43)$$

Being a special case of the co-volume scheme on non-orthogonal grids, the current scheme inherits the conservative properties from it, namely the conservation of PV dynamics and total energy.

## 5. Numerical results

In this section we present the results of numerical experiments conducted with the co-volume scheme (4.43) for the NSWSEs. The goals of these experiments are to demonstrate the convergence and the conservative properties of the scheme, and to address concerns about the scheme related to the computational modes and the possible decoupling between the system on the primary cells and the system on the dual cells. To these ends, we select the shallow water standard test cases #2 and #5 (SWSTC2 and SWSTC5, [24]), and a case with the doubly periodic domain. The analytic solutions of SWSTC2 allows accurate calculations of the numerical errors while the rich

dynamics in SWSTC5 allows qualitative evaluation of the computational modes. The doubly periodic case allows one to turn on and off the Coriolis parameter and assess the decoupling between the system on the primary cells and the systems on the dual cells.

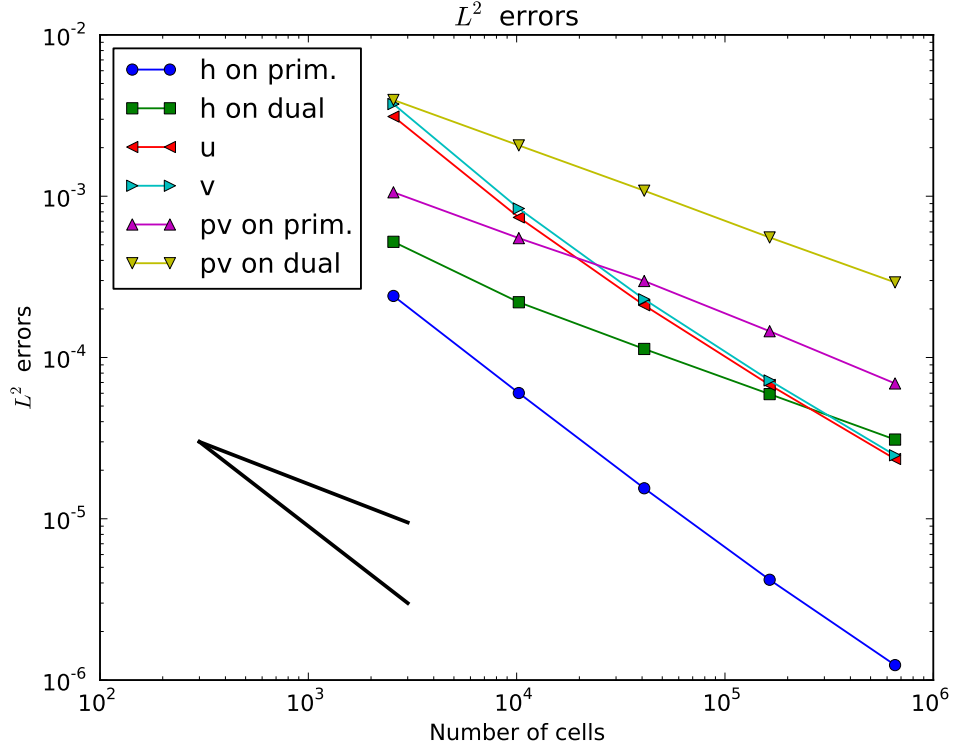


Figure 5.1: Convergence of the  $L^2$  errors in various variables for the SWSTC2. h: thickness; u: normal velocity components w.r.t. primary cells; v: tangential velocity components; pv: potential vorticity. Resolutions range from 480km to 30km.

#### *A case with nonlinear stationary solutions*

The SWSTC2 prescribes a geostrophically balanced zonal flow as the initial conditions for the nonlinear system (4.1), and thus the flow remains stationary and geostrophically balanced. The initial height and zonal velocity fields



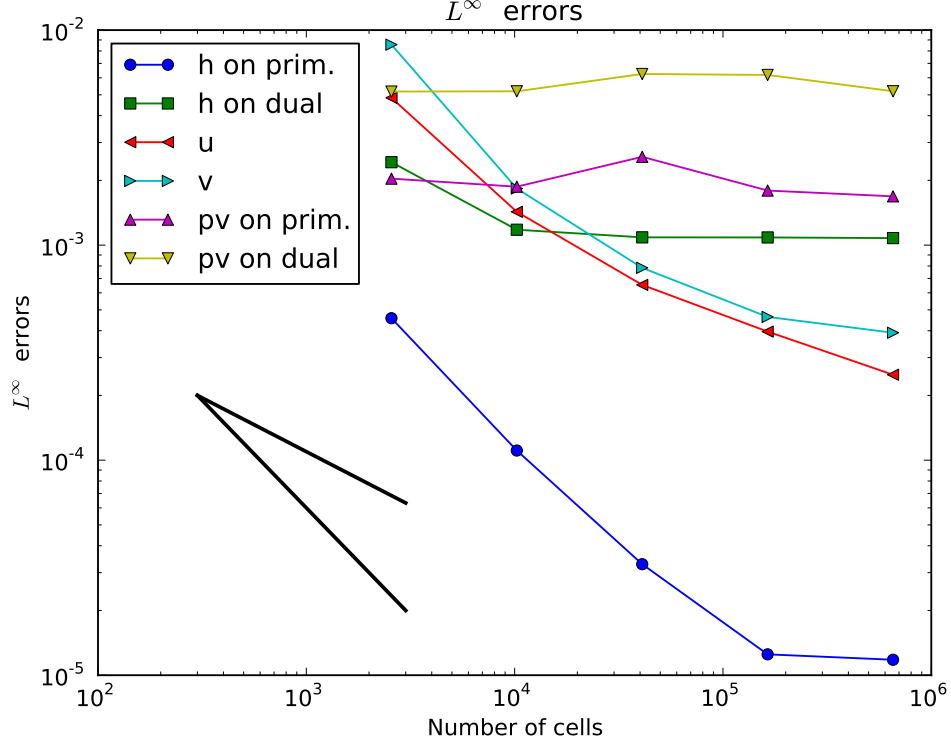


Figure 5.2: Convergence of the  $L^\infty$  errors in various variables for the SWSTC2. h: thickness; u: normal velocity components w.r.t. primary cells; v: tangential velocity components; pv: potential vorticity. Resolution range from 480km to 30km.

have the form

$$gh = gh_0 - \left( a\Omega u_0 + \frac{1}{2}u_0^2 \right) \cos \theta, \quad (5.1)$$

$$u = u_0 \cos \theta. \quad (5.2)$$

Following [24], we set the physical parameters as follows:  $\Omega = 7.292 \times 10^{-5} \text{s}^{-1}$  (earth rotation rate),  $g = 9.80616 \text{ms}^{-2}$  (gravity parameter),  $a = 6.37122 \times 10^6 \text{m}$  (earth radius),  $gh_0 = 2.94 \times 10^4 \text{m}^2 \text{s}^{-2}$  and  $u_0 = 2\pi a / (12 \text{ days})$ . The latitude is denoted by  $\theta$ .

In this experiment we use a set of global quasi-uniform spherical centroidal Voronoi tessellations (SCVT, [8]) with 2562, 10242, 40962 and 655362 cells, corresponding to resolutions of 480km, 240km, 120km, 60km and 30km re-

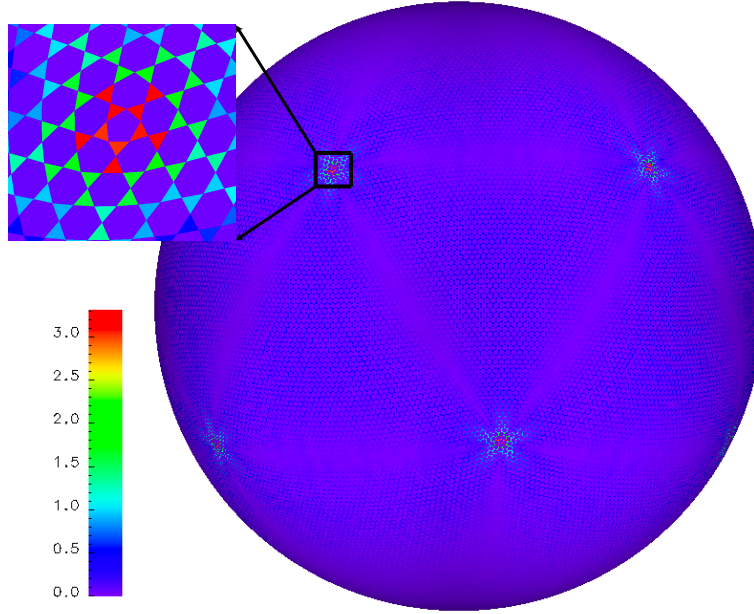


Figure 5.3: Errors in the thickness field from SWSTC2 on day 15 plotted on the non-overlapping E-grid from a spherical centroidal Voronoi tessellation. The unit for the errors is meter. The average thickness of the fluid is about 2000 meters.

spectively. A fourth order Runge-Kutta time stepping scheme is used with a step size of 172.8s.

We run the simulations for a period of 15 days, and plot in Fig. 5.1 and 5.2 the  $L^2$ - and  $L^\infty$ -norm, respectively, of the errors in fluid thickness, velocities and potential vorticity. On both figures, the reference first and second order convergence curves are included. In Fig. 5.1 we find that the  $L^2$ -norm of the errors in the fluid thickness variable at the primary cell centers and the  $L^2$ -norm of the errors in both velocity components converge consistently at a second-order rate. The  $L^2$ -norms of the errors in the potential vorticity variables at both the primary and dual cell centers converge consistently at the first order, which shouldn't be surprising because the potential vorticity (the relative vorticity, to be precise) involves first-order derivatives of the velocities. The  $L^2$ -norm of the errors in the fluid thickness variables at the dual cell centers also converges at a consistent first order rate. The reason for this downgraded convergence rate (compared to that for the thickness variable at the primary cell centers) is not fully understood. In the  $L^\infty$ -norm (Fig. 5.2), the errors in the fluid thickness variable at the primary

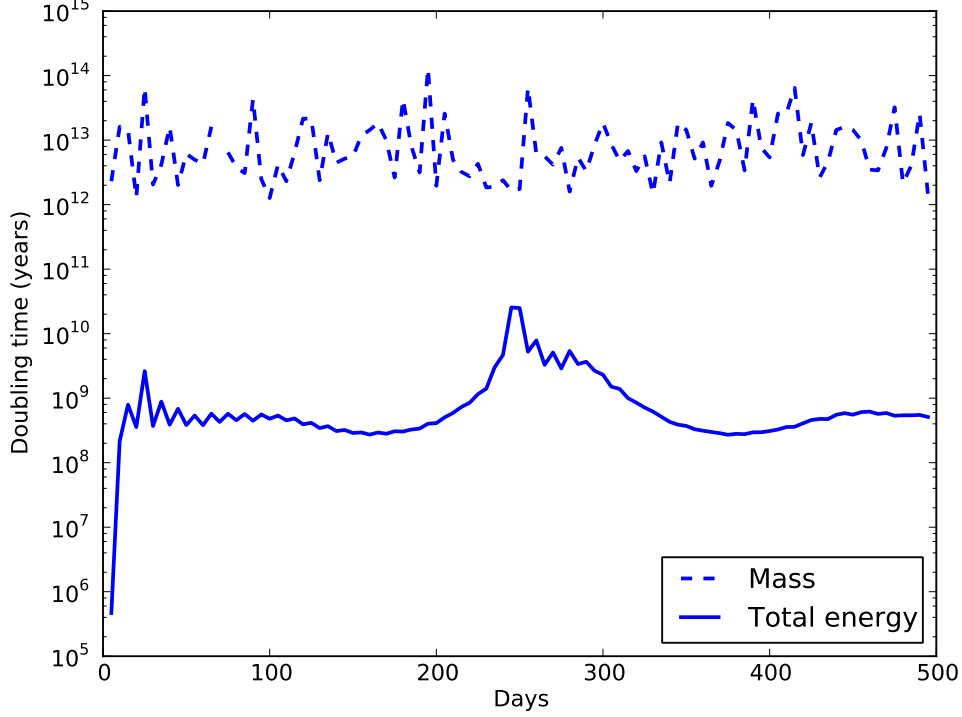


Figure 5.4: For the SWSTC2, the mass double time is on the order of  $10^{13}$  years, and the total energy (available potential energy + kinetic energy) doubling time is on the order of  $10^9$  years.

cell center and the errors in both of the velocity components do decrease as the mesh refines. Even though the convergence rates are not consistent among the resolutions considered. The errors in the fluid thickness variable at dual cell centers and the errors in the potential vorticity variables at both the primary and dual cell centers barely converge. The TRiSK scheme ([17]) involves only the thickness on the primary mesh, together with the normal velocity components, as the prognostic variables. On the SWSTC2, the scheme demonstrates a convergence order of 1.5 in the  $L^2$  norm for the thickness variable; the errors in the  $L^\infty$  norm barely converge (see Figure 7 therein). The performance of the co-volume on the thickness variable on the primary mesh, the same one as in TRiSK, should be considered favorably, however, it should also be kept in mind that its performance on the thickness

variable on the dual mesh is significantly degraded.

Figure 5.3 shows the distribution of errors in the thickness fields from both the primary and dual meshes on a global non-overlapping E-grid. Grid imprinting is evident in this global error field. This plot also confirms that the errors in the thickness field on the dual (triangular) mesh are more pronounced than on the primary mesh (c.f. Figures 5.1 and 5.2). In fact, the most severe errors come from the triangles around the few pentagonal cells.

By design, the co-volume scheme (4.43) conserves mass and absolute vorticity. It is also shown to conserve total energy. To demonstrate these conservative properties, we run a simulation of the SWSTC2 on the quasi-uniform 120km SCVT grid for a period of 500 days, and we examine the conservation of each of the three quantities mentioned above.

The stationary solutions of the SWSTC2 is meridionally symmetric, and therefore the flow has zero total absolute vorticity (TAV). For the discrete system (4.43) we compute the normalized total absolute vorticity (NTAV) as

$$\text{NTAV}_C = \frac{\sum_i h_i q_i A_i}{\sum_i A_i}, \quad (\text{TAV on primary cells}) \quad (5.3)$$

or

$$\text{NTAV}_V = \frac{\sum_\nu \tilde{h}_\nu \tilde{q}_\nu D_\nu}{\sum_\nu D_\nu}. \quad (\text{TAV on dual cells}) \quad (5.4)$$

Calculations using the data for the current simulation shows that both  $\text{NTAV}_C$  and  $\text{NTAV}_V$  are at the order of  $10^{-20}$ . Compared to the typical value  $10^{-5}$  of the Coriolis parameter, the non-zero  $\text{NTAV}_C$  and  $\text{NTAV}_V$  can be considered as round-off errors.

The total mass (TM) for the discrete system (4.43) is defined as

$$\text{TM} = \sum_i h_i A_i.$$

For long-term simulations, a telling indicator of the mass conservativeness of a numerical scheme is the time needed for the doubling of the system's total mass. We calculate the total mass doubling time (TMDT) as

$$\text{TMDT} = \frac{\text{TM} * \Delta t}{|[TM]|},$$

where  $\Delta t$  denotes the time step size and  $[TM]$  the change in total mass between two time steps. For this experiment, the TM holds virtually constant

over the whole simulation period; the TMDT is at the order of  $10^{13}$  years (Fig. 5.4), more than enough for any realistic applications.

The total energy (TE) is defined as the sum of the *available potential energy* (APE) and the kinetic energy (KE), that is,

$$\text{TE} = \sum_e \bar{h}_e \bar{A}_e \bar{K}_e + \frac{1}{2} \left( \sum_i \frac{1}{2} g A_i (h_i - \bar{h})^2 + \sum_\nu \frac{1}{2} g A_\nu (\tilde{h}_\nu - \bar{h})^2 \right), \quad (5.5)$$

where  $\bar{h}$  is the average fluid thickness. As for the total mass, we calculate the total energy doubling time (TEDT) as

$$\text{TEDT} = \frac{\text{TE} * \Delta t}{|[\text{TE}]|},$$

where  $[\text{TE}]$  is the change in total energy between two time steps. Again, over the whole simulation period, the TE holds virtually constant; the TEDT is at the order of  $10^9$  years (Fig. 5.4).

*A case with mountain topography*

The SWSTC5 ([24]) involves a zonal flow impinging on a mountain. The initial zonal velocity  $u$  of the flow and the surface height  $\tilde{h}$  are given by

$$u = u_0 \cos \theta, \\ g\tilde{h} = gh_0 - \left( a\Omega u_0 + \frac{u_0^2}{2} \right) \cos \theta,$$

respectively. The mountain, as part of the lower boundary, has the form

$$b = b_0 \left( 1 - \frac{r}{R_0} \right).$$

The fluid thickness  $h$  is then give by

$$h = \tilde{h} - b.$$

In the above,  $\theta$  represents the latitude as usual, and the other physical parameters are set following [24], namely,  $\Omega = 7.292 \times 10^{-5} \text{s}^{-1}$ ,  $g = 9.80616 \text{ms}^{-2}$ ,  $a = 6.37122 \text{m}$ ,  $u_0 = 20 \text{ms}^{-1}$ ,  $h_0 = 5960 \text{m}$ ,  $b_0 = 200 \text{m}$ ,  $R_0 = \pi/9$ ,  $r^2 = \min[R_0^2, (\lambda - \lambda_c)^2 + (\theta - \theta_c)^2]$ , with  $\lambda$  denoting the longitude and  $\lambda_c = -\pi/2$ ,  $\theta_c = \pi/6$ . For this test case we use a generic fourth order Runge-Kutta scheme with a step size of 172.8s.

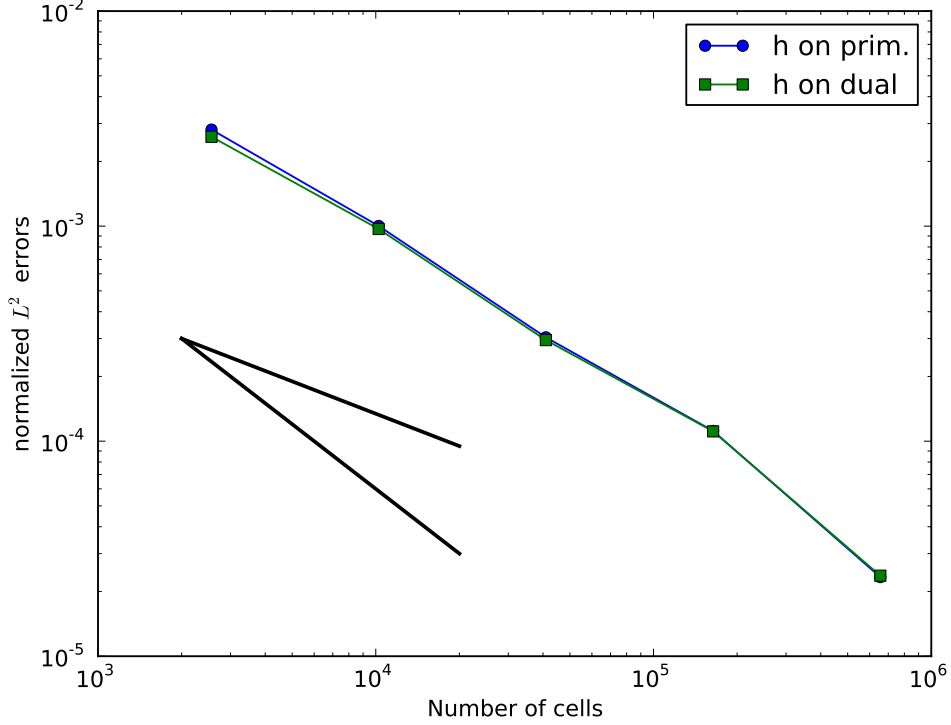


Figure 5.5: Convergences of the  $L^2$  errors in the thickness variables on primary cells and the thickness variables on dual cells for the SWSTC5. Resolutions range from 480km to 30km.

There are no known analytic solutions to the SWSTC5. What are available, instead, are high-resolution reference solutions by spectral methods ([19]). To study the convergence of the co-volume scheme on SWSTC5, we run the test case again on a set of global SCVT grids with 2562, 10242, 40962, 163842 and 655362 cells, corresponding to resolutions of 480km, 240km, 120km, 60km and 30km. We then compare the fluid thickness variables, both at the primary cell centers and at the dual cell centers, to the spectral T511 high-resolution reference solutions of SWSTC5. The  $L^2$ -norms of the errors on day 15 are computed and plotted in Fig. 5.5 against the number of cells, which is proportional to the resolutions. We find that the thickness variables on the primary cell centers and the thickness variables on the dual cell centers are equally accurate, and both converge to the reference

solutions at approximately the second order (c.f. the reference convergence curves) throughout the whole range of resolutions used for this study. This result is similar to that of [17] (Fig. 8 therein).

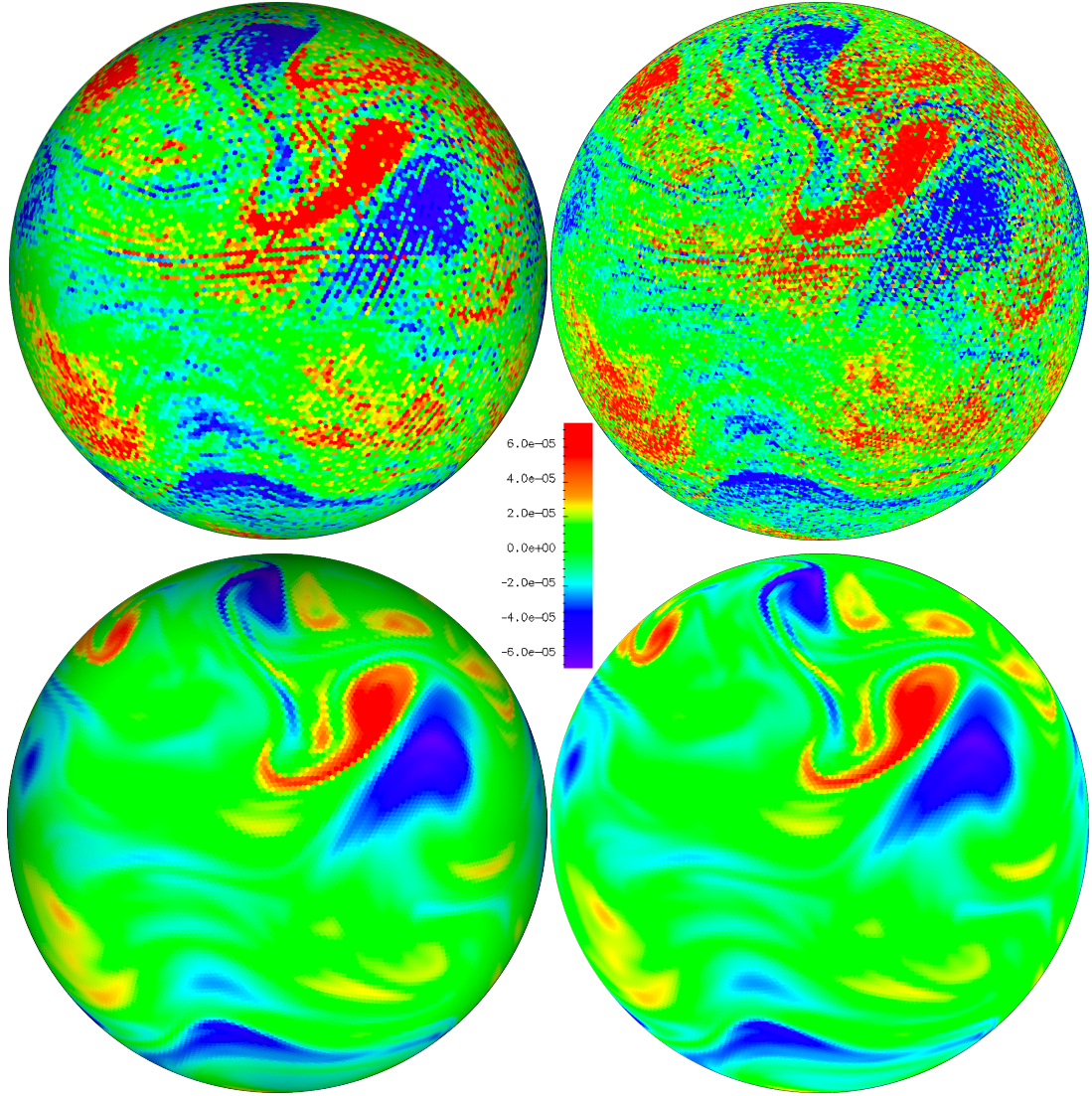


Figure 5.6: Snapshot of the relative vorticity (RV) field on day 50 for the SWSTC5. Top left: RV on hexagons, no diffusion. Top right: RV on triangles, no diffusion. Bottom left: RV on hexagons, with the  $\nabla^4$  diffusion of  $1.6e^{14}$ . Bottom right: RV on triangles, with the  $\nabla^4$  diffusion of  $1.6e^{14}$ .



The mountain topography of SWSTC5 serves as an inhomogeneity that gradually breaks down the symmetry of the flow, and it is known that the flow evolves into turbulence in around 25 days. We run the SWSTC5 on the 40962-cell (res. 120km) SCVT, first without any diffusion and then with a biharmonic diffusion, for 50 days. In Figure 5.6 are the snapshots of the relative vorticity field from these two simulations on day 50. All plots are made on the same colormap (shown in the figure) to emphasize the large-scale structures shared among them. For the inviscid simulation, the vorticity field on the triangular mesh (top right) appears slightly than the vorticity field on the hexagonal mesh (top left). The stripy grid-scale oscillation in the vorticity field on the hexagonal mesh could be the manifestation of a spurious computational mode, as we recall that the vorticities on the hexagonal mesh are defined by the normal velocity components on the triangular mesh (see (4.17)), which has been shown to support one spurious mode (see (3.17)). With a biharmonic diffusion of  $1.6 \times 10^{14} \text{m}^4 \text{s}^{-1}$ , which is typical at this level of resolutions, the noises and the oscillations, for both the hexagonal and triangular meshes, are largely suppressed. In this study we only experiment with the basic biharmonic diffusions. Currently there is active research on advanced advection schemes (see e.g. [6, 5, 23]) that can control the computational modes without much damage on the large-scale structures. These options will be explored in our future work.

*A case with a doubly periodic domain.*

The SWSTC2 and 5 has a Rossby deformation radius of about 2,000km at the mid-latitudes, which is well resolved by virtually all shallow water models. However, in a realistic ocean, the higher internal baroclinic modes have much smaller equivalent depths, and accordingly much smaller *baroclinic Rossby deformation radii* ([10]). For example, the typical values for the Rossby deformation radius of the first baroclinic modes of the ocean are 10-30km (again see [10]), which is, at the best, only marginally resolved by the present-day cutting-edge high resolution ocean models. When the Rossby deformation radius is not well resolved, the performance of many numerical schemes, including the popular C-grid schemes are severely downgraded. This challenge motivates [9] to explore the merits of various numerical schemes on both the hexagonal and triangular meshes. Here we construct a test case that is very similar to the one in [9] in that it has a very small Rossby deformation radius, and we examine how spurious modes can affect our co-volume scheme under the circumstance that the Rossby deformation radius is not resolved.

Due to its double-system nature, another potential concern about the co-volume scheme is that the two subsystems may drift far too apart. In a subsequent experiment with this test case (but with a minor change in one parameter) , we want to numerically assess the drifting. This idealized setting allows us to push the case to the extreme by assuming a vanishing Coriolis parameter, which leads to a complete decoupling between the subsystem  $(h, u)$  and the subsystem  $(\tilde{h}, v)$  in the scheme(3.5) for the linearized shallow water equations. This modified setting is still physically relevant, as it resembles the narrow region along the equator.

The test case is set in a  $2,000\text{km} \times 1,732\text{km}$  doubly periodic domain. At  $t = 0$ , the surface height of the flow is given by

$$h_0(x, y) = 0.408 + 0.02e^{-\left[\left(\frac{x-x_c}{2.5r}\right)^2 + \left(\frac{y-y_c}{r}\right)^2\right]},$$

with  $(x_c, y_c) = (1,000\text{km}, 866\text{km})$  being the center of the domain and  $r = 160\text{km}$  the radius of the perturbation region. The Coriolis parameter is set to a constant  $f = 10^{-4}$ , and therefore the flow has a Rossby deformation radius of approximately  $R = 20\text{km}$ . The initial velocity field is set to zero,  $\mathbf{u}_0(x, y) = 0$ . This choice is non-essential, as the flow will be engaged in geostrophic adjustment.

On a uniform hexagon-triangular staggered grid of resolution  $d = 40\text{km}$ , we have  $R/d = 0.5$ , the same ratio that [9] takes. We use a fourth order Runge-Kutta scheme with a step size of 720s, and plot in Figure 5.7 the divergence field after 400 time steps (about 3 days) on both the hexagonal and triangular meshes. Due to the coarseness of the meshes, the cell shapes are evident on both plots. Nonetheless, the divergence field on the hexagonal mesh is non-oscillatory, and its structure is coherent. No checkboard noise or other spurious modes are seen. On the triangular mesh, the divergence field appears oscillatory along the contact lines between positive and negative regions. This is probably due to the grid structure on the triangular mesh, where the centers of neighboring triangles are not at the same level. No computational modes are seen at this stage.

To assess the possible decoupling between the fields on the primary mesh and the fields on the dual mesh, we calculate and the plot the normalized  $L^2$ -norm of the difference between the thickness fields on the two meshes, both with a non-zero Coriolis parameter and with a vanishing Coriolis parameter. The discrete variables  $h_i$  and  $\tilde{h}_\nu$  cannot be directly compared because they are defined on different and non-overlapping grid points. To circumvent this

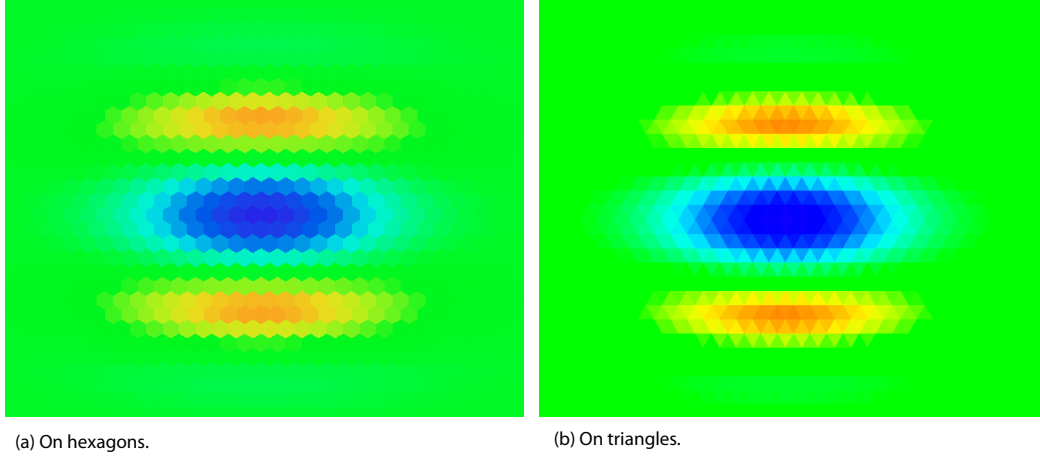


Figure 5.7: The divergence field on the hexagons and the triangles after 400 time steps (around day 3). Both figures are on the identical color scale, and are showing the same region of the domain (zonal (400km, 1600km) X meridional (360km, 1440km)).

technical difficulty we first interpolate  $h_i$  on the dual cell centers, call the new discrete variables  $\hat{h}_\nu$ , and then compare them with  $\tilde{h}_\nu$ , and compute the normalized  $L^2$ -norm of the difference between these two fields as

$$\frac{\sqrt{\sum_\nu A_\nu (\hat{h}_\nu - \tilde{h}_\nu)^2}}{\sqrt{\sum_\nu A_\nu \tilde{h}_\nu(t=0)^2}}.$$

We note that, on a hexagon-triangular grid with the primary and dual meshes referring to the hexagons and triangles respectively, there are twice as many triangles as there are hexagons. When a field is mapped from its native mesh to another mesh with higher resolution, none of its defects will be hidden or filtered out, and this makes the subsequent comparison most revealing of the defects in the data.

In Figure 5.8 we plot the time evolution of the  $L^2$ -norm of the difference between  $h$  ( $\hat{h}$  to be precise) and  $\tilde{h}$ , for each of the grids used. The plots are set on a semi-log scale to reveal the relation between the difference and the grid resolution at any given time. The left panel (a) shows that, with a non-zero Coriolis parameter, the difference between two thickness fields does not increase over time for each of the grids considered, and at any fixed time, the difference between the two fields converges at a second order with respect to the grid resolutions, which is the optimal convergence rate

of the co-volume scheme with respect to the grid resolutions. In contrast, on the right panel (b) for the case with a vanishing Coriolis parameter, the difference between  $h$  and  $\tilde{h}$  on each grid grows linearly in time. Based on linear extrapolation, the  $L^2$  errors will be as large as the mean field in about 150,000 days. Again, it is seen in this case that, at any fixed time, the difference between the two fields converges towards zero at a roughly second order with respect to the grid resolutions. The fact that the difference between  $h$  and  $\tilde{h}$  converges at the optimal convergence order of the numerical scheme for both the zero- and non-zero-Coriolis cases suggests that the difference between the two fields are directly correlated to the numerical errors in them. In other words, the divergence between the two fields is not substantial for both cases. That the difference between the two fields grows linearly in time for the zero-Coriolis case should not come as a surprise, as the numerical errors in a discrete system are expected to grow, linearly in time for most cases. That the difference between the fields remains relatively constant for the non-zero-Coriolis case may be attributed to the outstanding performance of the co-volume scheme in resolving the slow geostrophic adjustments in this case.

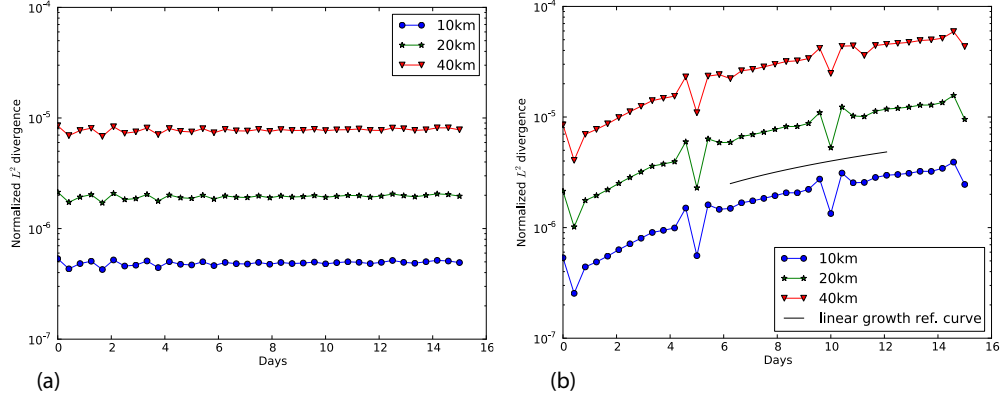


Figure 5.8: The growth of the difference between  $h_i$  and  $\tilde{h}_t$ , for a case on a doubly periodic domain: (a) with a non-zero Coriolis parameter  $f = 10^{-4}$ , and (b) with a vanishing Coriolis parameter.

## 6. Concluding remarks

The co-volume scheme specifies both the normal and tangential velocity components on the edges and evolve fluid thickness on both the primary and dual cell centers. It can be viewed as coupled C-grid schemes on the primary and dual meshes, or as a generalization of the E-grid scheme onto an unstructured mesh connecting the velocity points. On a uniform quadrilateral staggered grid, the scheme possesses the same dispersive relation as that of the Z-grid scheme on a subset of the resolved wavenumber space associated with either the primary or the dual mesh. Outside this subset, the co-volume scheme behaves like an E-grid. The co-volume scheme achieves this performance without the burden of globally inverting elliptic equations, but at the cost of evolving a double-sized system compared to the classical C-grid scheme. On the uniform hexagon-triangular staggered grid, the co-volume scheme has two inertial-gravity wave modes on each of the hexagonal and the triangular meshes, and two spurious computational modes on the triangular mesh. The inertial-gravity modes remain monotonically increasing even when the Rossby deformation radius is under-resolved. These wave modes, including both the inertial-gravity and the spurious modes, account for about half of the wavenumber space resolvable on the hexagon-triangular grids. We do not know whether the dispersive relations on the unidentified wavenumber space are benign or not. Numerical experiments with the NSWEE demonstrate that the co-volume scheme achieves a consistent second-order convergence rate for the prognostic variables on the primary mesh, and conservation of mass, energy and potential vorticity up to time truncation errors.

The co-volume scheme is algorithmically most close to the TRiSK scheme. These schemes can also operate on the same type of grids, although the co-volume scheme is applicable to a much wider class of grids. Therefore, it is tempting to compare these two schemes in terms of efficiency. The co-volume scheme specifies prognostic variables  $h$  and  $u$  on the primary mesh and  $\tilde{h}$  and  $v$  on the dual mesh, together with diagnostic variables  $q$  and  $\tilde{q}$  etc. The prognostic variables are advanced simultaneously on both the primary and dual meshes. The TRiSK is a C-grid scheme with the prognostic variables  $h$  and  $u$  on the primary mesh, but it also defines diagnostic variables, e.g.  $\tilde{h}$  and  $\tilde{q}$ , on the dual mesh. These variables are diagnosed from the prognostic variables at each time step. In addition, at every time step, the tangential velocity components  $v$ , defined on the edges, are reconstructed from the

normal velocity components  $u$  according to mapping scheme set forth in [21], which itself is an expensive process. Due to these extra calculations that TRiSK needs to carry out besides advancing the prognostic variables, we expect that the co-volume and the TRiSK schemes should be comparable in terms of efficiency. Numerical tests with both schemes using the SWSTC5 and an explicit fourth order Runge-Kutta time stepping technique confirm this conclusion. When these schemes are applied to a three dimensional model, an implicit or a split-explicit time stepping technique will likely be used. We do not foresee that these advanced stepping techniques will make one scheme more efficient than the other, but more analysis and numerical experiments are certainly warranted.

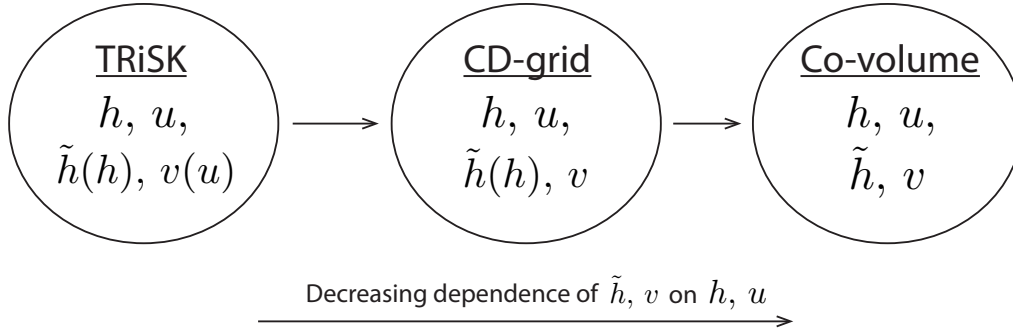


Figure 6.1: Diagram on the relation between the TRiSK, CD-grid and co-volume schemes.

The co-volume scheme for the NSWE, on both orthogonal and non-orthogonal grids, requires the values of the thickness and the potential vorticity on the edges, the thickness for computing the thickness fluxes, and the thickness and the potential vorticity for computing the nonlinear Coriolis terms. We obtain an approximation to each of these variables by taking the mean of its values on neighboring primary and dual cell centers. This choice has served us well in the sense that it leads to mostly a second-order convergence for the state variables on quasi-uniform SCVT grids and that it ensures preservation of PV dynamics and conservation of energy up to time truncation errors on both orthogonal and non-orthogonal grids. However, a smarter reconstruction of each of these variables on the edges, taking local inhomogeneity into account and differentiating between its values along the primary cell edge and the dual cell edge, is expected to help the co-volume scheme on non-orthogonal grids to achieve an improved and consistent convergence rate. This subject is left for future explorations.

Another related issue, which is also a potential subject of further endeavors, is about the advection scheme for the thickness and the PV variables. The current work lays down the framework for constructing co-volume schemes for SWEs and explores the potential of these schemes in climate applications through linear wave analysis and numerical experiments. In the next step, various advection schemes, for example, the Monotone Upstream-centered Schemes for Conservation Laws (MUSCL, [22]) and the continuous, linear-upwind stabilised transport (CLUST, [23]), will be explored. These advanced advection schemes are expected to improve the overall accuracy of the scheme and/or control the computational modes.

The C-grid TRiSK scheme and the CD-grid scheme of [1] can both be cast in the co-volume framework. These two schemes and the co-volume scheme are distinguished by the level of dependence of the dual variables  $\tilde{h}$  and  $v$  on the primary variables  $h$  and  $u$ . We denote such dependence by writing the dependent variable as a function of the independent variable, e.g.  $\tilde{h}(h)$ . The diagram in Figure 6.1 illustrates the dependence among its variables for each of the three schemes and the relation between them. In TRiSK, both of the dual variables  $\tilde{h}$  and  $v$  are diagnosed from the primary variables  $h$  and  $u$ , i.e. the dual variables are completely dependent on the primary variables. In the CD-grid scheme, only the dual thickness variable  $\tilde{h}$  is dependent on the primary thickness variable; the tangential velocity component is independent of the normal velocity component. The co-volume scheme represents the extreme case in which the primary variables  $h$  and  $u$  and the dual variables  $\tilde{h}$  and  $v$  are treated independently. In this article we present the co-volume scheme as it stands. Numerical results demonstrate that it is a competitive option towards simulations of geophysical flows. Modifications to the scheme are certainly possible. For example, the dual variables  $\tilde{h}$  and  $v$  can be made to be *partially* dependent on the primary variables  $h$  and  $u$ . This will lead to stronger coupling between the two subsystems on the primary and dual meshes. It may also mitigate the spurious modes on the dual mesh. Such modifications will be explored in our future work.

The co-volume scheme also has a few key advantages that should stimulate further research on this method. The scheme is applicable to non-orthogonal grids. We derive the general form of the numerical scheme for the NSWE on non-orthogonal grids. In this work we only evaluate the merits of the scheme on orthogonal grids. We believe that to tell a whole story about the scheme on non-orthogonal grids requires significant amount of effort and space, and is better left for a separate endeavor. Another advantage of the co-

volume scheme is that the presence of both velocity components on the edges should enhance the capability of the scheme to deal with complex boundaries. One idea is, in the case of hexagon-triangular grids, to align the triangles with the boundaries. It is known that triangular meshes can accurately represent the boundaries of complex geometries. In contrast, hexagonal meshes, used by schemes like TRiSK, tend to have unrealistic jigsaws along the ocean-land boundaries. Finally, the real world ocean or atmosphere has many baroclinic modes with small equivalent depths and hence small baroclinic Rossby deformation radii that are not resolved in current global circulation models (see discussion in the doubly periodic test case in the last section). It has been shown that the co-volume scheme maintains a monotonically increasing inertial-gravity modes on both the hexagonal and triangular meshes even when the Rossby deformation radius is not resolved, and it will be interesting to see what impacts does the scheme has on three-dimensional ocean or atmosphere simulations.

## References

- [1] A J Adcroft, C N Hill, and J C Marshall, *A New Treatment of the Coriolis Terms in C-Grid Models at Both High and Low Resolutions*, Monthly Weather Review **127** (1999), 1928–1936.
- [2] A. Arakawa and V. R. Lamb, *Computational design of the basic dynamical processes of the UCLA General Circulation Model*, Methods Comput. Methods in computational physics **17** (1977), 173–265.
- [3] ———, *A potential enstrophy and energy conserving scheme for the shallow water equations*, Monthly Weather Review **109** (1981), no. 1, 18–36.
- [4] Lisa A. Baughman and Noel J. Walkington, *Co-volume methods for degenerate parabolic problems*, Numer. Math. **64** (1993), no. 1, 45–67.
- [5] Q. Chen and M Gunzburger, *A Scale-Aware Anticipated Potential Vorticity Method. Part II: on Variable-Resolution Meshes*, Monthly Weather Review, in press.
- [6] Qingshan Chen, Max Gunzburger, and Todd Ringler, *A Scale-Invariant Formulation of the Anticipated Potential Vorticity Method*, Monthly Weather Review **139** (2011), no. 8, 2614–2629.



- [7] S. Danilov, *On utility of triangular C-grid type discretization for numerical modeling of large-scale ocean flows*, Ocean Dynamics (2010), 1–9.
- [8] Qiang Du, Max D. Gunzburger, and Lili Ju, *Constrained centroidal Voronoi tessellations for surfaces*, SIAM Journal on Scientific Computing **24** (2003), no. 5, 1488–1506 (electronic).
- [9] Almut Gassmann, *Inspection of hexagonal and triangular C-grid discretizations of the shallow water equations*, Journal of Computational Physics **230** (2011), no. 7, 2706–2721.
- [10] Adrian E. Gill, *Atmosphere-Ocean Dynamics*, International Geophysics Series, vol. 30, Academic Press, 1982.
- [11] Christopher A. Jeffery, *Assessment of model errors in limited-area simulations of shallow water test cases on the C-grid plane and sphere*, in preparation.
- [12] Daniel Y Le Roux, Virgile Rostand, and Benoit Pouliot, *Analysis of Numerically Induced Oscillations in 2D Finite-Element Shallow-Water Models Part I: Inertia-Gravity Waves*, SIAM Journal on Scientific Computing **29** (2007), no. 1, 331.
- [13] S.J. Lin and R.B. Rood, *An explicit flux-form semi-Lagrangian shallow-water model on the sphere*, Quarterly Journal of the Royal Meteorological Society **123** (1997), no. 544, 2477–2498.
- [14] R. A. Nicolaides, *The covolume approach to computing incompressible flows*, Incompressible computational fluid dynamics: trends and advances, Cambridge Univ. Press, Cambridge, 2008, pp. 295–333.
- [15] Roy A. Nicolaides and Xiaonan Wu, *Covolume Solutions of Three-Dimensional Div-Curl Equations*, SIAM Journal on Numerical Analysis **34** (1997), no. 6, pp. 2195–2203.
- [16] D.A. Randall, *Geostrophic adjustment and the finite-difference shallow-water equations*, Monthly Weather Review **122** (1994), no. 6, 1371–1377.
- [17] T. D. Ringler, J Thuburn, J. B. Klemp, and W. C. Skamarock, *A unified approach to energy conservation and potential vorticity dynamics for arbitrarily-structured C-grids*, Journal of Computational Physics **229** (2010), no. 9, 3065–3090.

- [18] William C. Skamarock, *A Linear Analysis of the NCAR CCSM Finite-Volume Dynamical Core*, Monthly Weather Review **136** (2008), no. 6, 2112–2119.
- [19] PN Swarztrauber, *Spectral transform methods for solving the shallow-water equations on the sphere*, Monthly Weather Review **124** (1996), no. 4, 730–744.
- [20] J Thuburn, *Numerical wave propagation on the hexagonal C-grid*, Journal of Computational Physics **227** (2008), no. 11, 5836–5858.
- [21] J Thuburn, TD Ringler, WC Skamarock, and JB Klemp, *Numerical representation of geostrophic modes on arbitrarily structured C-grids*, Journal of Computational Physics **228** (2009), no. 22, 8321–8335.
- [22] Bram van Leer, *Towards the ultimate conservative difference scheme. V. A second-order sequel to Godunov’s method*, Journal of Computational Physics **135** (1997), no. 2, 227–248.
- [23] H Weller, *Controlling the Computational Modes of the Arbitrarily Structured C-grid*, Monthly Weather Review, in press.
- [24] David L Williamson, John B Drake, James J Hack, Rüdiger Jakob, and Paul N. Swarztrauber, *A standard test set for numerical approximations to the shallow water equations in spherical geometry*, Journal of Computational Physics **102** (1992), no. 1, 211–224.
- [25] F Xiao, X D Peng, and X S Shen, *A Finite-Volume Grid Using Multimoments for Geostrophic Adjustment*, Monthly Weather Review **134** (2006), no. 9, 2515–2526.